Volcanic Flank Collapse, Secondary Sediment Failure and Flow-Transition: Multi-Stage Landslide Emplacement Offshore Montserrat, Lesser Antilles

Michel Kühn[1,2] , Christian Berndt[1] , Sebastian F. L. Watt[3] , Matthew J. Hornbach[4,5], Sebastian Krastel[2] , Kristina Sass[6] , Steffen Kutterolf[1] , Tim Freudenthal[6], Katrin Huhn[6], Jens Karstens[1] , Bettina Schramm[7], Judith Elger[1] , Christoph Böttner[8], and Dirk Klaeschen[1]

[1]GEOMAR Helmholtz Centre for Ocean Research Kiel, Kiel, Germany, [2]Institute of Geosciences, Kiel University, Kiel, Germany, [3]School of Geography, Earth and Environmental Sciences, University of Birmingham, Birmingham, UK, [4]Huffington Department of Earth Sciences, Southern Methodist University, Dallas, TX, USA, [5]United States Naval Research Laboratory, Stennis Space Center, MS, USA, [6]MARUM, University of Bremen, Bremen, Germany, [7]Federal Institute for Geosciences and Natural Resources, Hannover, Germany, [8]Institute for Geoscience, Aarhus University, Aarhus, Denmark

Abstract Volcanic flank collapses, especially those in island settings, have generated some of the most voluminous mass transport deposits on Earth and can trigger devastating tsunamis. Reliable tsunami hazard assessments for flank collapse-driven tsunamis require an understanding of the complex emplacement processes involved. The seafloor sequence southeast of Montserrat (Lesser Antilles) is a key site for the study of volcanic flank collapse emplacement processes that span subaerial to submarine environments. Here, we present new 2D and 3D seismic data as well as MeBo drill core data from one of the most extensive mass transport deposits offshore Montserrat, which exemplifies multi-phase landslide deposition from volcanic islands. The deposits reveal emplacement in multiple stages including two blocky volcanic debris avalanches, secondary seafloor failure and a late-stage erosive density current that carved channel-like incisions into the hummocky surface of the deposit about 15 km from the source region. The highly erosive density current potentially originated from downslope-acceleration of fine-grained material that was suspended in the water column earlier during the slide. Late-stage erosive turbidity currents may be a more common process following volcanic sector collapse than has been previously recognized, exerting a potentially important control on the observed deposit morphology as well as on the runout and the overall shape of the deposit.

Plain Language Summary Disintegration of volcanic islands can cause very large landslides and destructive tsunamis. To assess the tsunami hazard of such events, it is crucial to understand the processes that are involved in their formation. We present new insights from seismic data and drill cores from a landslide deposit offshore Montserrat, a volcanic island in the Lesser Antilles Arc in the Caribbean. Our analysis reveals the emplacement of landslide material in several stages, including multiple volcanic flank collapses, incorporation of seafloor sediments and an erosive flow that carved channels into the top of the deposit right after its emplacement. We suggest that highly erosive flows are a common process during volcanic flank collapse deposition and that they play a significant role in the shaping of the deposit's appearance.

1. Introduction

The devastating tsunamigenic collapse of Anak Krakatau, Indonesia, in December 2018 emphasized the potential of volcanic sector collapses to threaten coastal communities and infrastructure around volcanic islands. In the last 200 years, volcanic sector collapses have produced several destructive tsunamis and caused thousands of casualties around the world (Auker et al., 2013; Watt et al., 2021). The Anak Krakatau collapse in 2018 led to a tsunami with runup heights of up to 13 m at the coast of the Sunda Strait (Walter et al., 2019), even though the slide volume of 0.2–0.3 km^3 (Grilli et al., 2019) was relatively small in the context of many of the pre-historical sector collapse deposits mapped offshore volcanic islands globally (e.g., Moore & Normark, 1994). The largest historical tsunamigenic sector collapse was that at Ritter Island, Papua New Guinea, in 1888 (Ward & Day, 2003), which had an initial collapse volume of 2.4 km^3 (Karstens et al., 2019), while the geological record from offshore other volcanic islands revealed deposits involving tens or even hundreds of cubic kilometers of material (Krastel et al., 2001; Masson et al., 2002, 2006). However, the tsunami potential of a volcanic landslide is not solely

controlled by the volume of the sliding mass but is influenced by both emplacement dynamics and bathymetric controls.

The emplacement of volcanic island flank collapse deposits on the adjacent seafloor involves a complex interplay of different geological processes, influenced by the dimensions, lithologies, geometry and position of this initial failure of the flank (in some instances subaerially), the extent of disintegration of the flank material, the interaction of the failed mass with the substrate, including the entrainment of pre-existing seafloor materials, and the runout, deceleration and compression of the distal collapse-derived deposits (Karstens et al., 2019; Masson et al., 2006; Watt et al., 2019). Given this complexity, collapse deposit morphology and volume cannot be related to tsunamigenic potential in a simple way. The most important controls on the magnitude of a collapse-generated tsunami are parameters such as the initial volume of the collapsing flank and its initial slide velocity during failure and emplacement relative to water depth (Karstens et al., 2020; Løvholt et al., 2015; Ward, 2001). For adequate tsunami hazard assessments, we therefore need to understand how a submarine landslide changes size and velocity in both space and time during failure. In particular, for ancient flank collapse deposits, without independent tsunami observations, a full understanding of tsunamigenic potential is reliant on being able to connect depositional characteristics and processes to tsunami generation. However, the characteristics (e.g., the origin from a single collapse vs. the origin from multiple collapse events) of those deposits may obscure the original landslide parameters (e.g., final or total deposit volume vs. the initial volcanic flank collapse volume). Potential complexities in mass transport deposit emplacement include determining whether a collapse was a single- or multiphase event (Karstens et al., 2019, 2020; Watt et al., 2019), if secondary seafloor failure occurred (Barrett et al., 2020; Brunet et al., 2016; Crutchley et al., 2013; Le Friant et al., 2015), how much seafloor sediment was incorporated into the slide mass (Kühn et al., 2021; Ogata et al., 2019), and if more than one collapse event led to the final mass transport deposit.

Here, we present an extensive new data set for one of the best studied submarine mass transport deposits resulting from volcanic flank collapse: Deposit 2 offshore Montserrat, Lesser Antilles (Lebas et al., 2011; Watt, Talling, Vardy, Heller, et al., 2012). Deposit 2 is an elongated deposit showing indications for a volcanic flank collapse (Watt et al., 2015), secondary failure of preexisting seafloor sediments (Crutchley et al., 2013), and has also been separated into two subunits (2a/2b) by interpretation of an internal package of continuous reflections, suggesting that the deposit originated via at least two separate landslide events (Lebas et al., 2011; Watt, Talling, Vardy, Heller, et al., 2012, Watt, Talling, Vardy, Masson, et al., 2012). To advance our understanding of Deposit 2, as an exemplar of a complex mass transport deposit offshore a volcanic island, we combine high-resolution 2D and 3D seismic reflection data, sediment echosounder data and bathymetry with MeBo70 drill cores. The objectives are to re-evaluate the delimitation of individual events represented within Deposit 2 and to constrain the geological processes that produced these. Particular emphasis is put on the relative timing and interplay of these processes.

2. Geological Background

The island of Montserrat is located in the northern part of the Lesser Antilles volcanic arc, NW of Guadeloupe and SW of Antigua (Figure 1, inset). The northern Lesser Antilles arc is formed by the subduction of the North American plate beneath the Caribbean plate with a present-day subduction rate of 2–4 cm/a (Bouysse & Westercamp, 1990; Grindlay et al., 2005). Volcanism on Montserrat migrated southward over time, from Silver Hills volcano in the north (2.6 Ma), via Center Hills in the center of the island (0.95–0.55 Ma) to Soufrière Hills (alongside the South Soufrière Hills cone) <0.17 Ma (Davis, 1924; Harford et al., 2002). The mainly andesitic Soufrière Hills most recently erupted between 1995 and 2010 (Wadge et al., 2014). This eruption produced a long-lived lava-dome that underwent several partial collapses, devastating large parts of the island and burying the capital, Plymouth, under extensive pyroclastic deposits (Young et al., 1998). The eruption and collapse history of the Soufrière Hills from 1995 onwards has been intensively documented (Herd et al., 2005; Le Friant et al., 2009; Sparks et al., 2002; Young et al., 1998).

The offshore topography SE of Montserrat is formed by the NNW-SSE striking Montserrat-Bouillante-Graben (Figure 1; in the following, *M-B-Graben*), which is bordered to the SW by the Montserrat-Bouillante-Les Saints Fault System, to the NE by the Kahouanne Seamounts (Feuillet et al., 2010), and to the north by a broadly west-east striking headwall scarp (Crutchley et al., 2013).

Several surficial and buried mass transport deposits (Le Friant et al., 2004; Lebas et al., 2011) as well as pyroclastic flow deposits and turbidites have been mapped out around Montserrat in seismic, bathymetry and core data
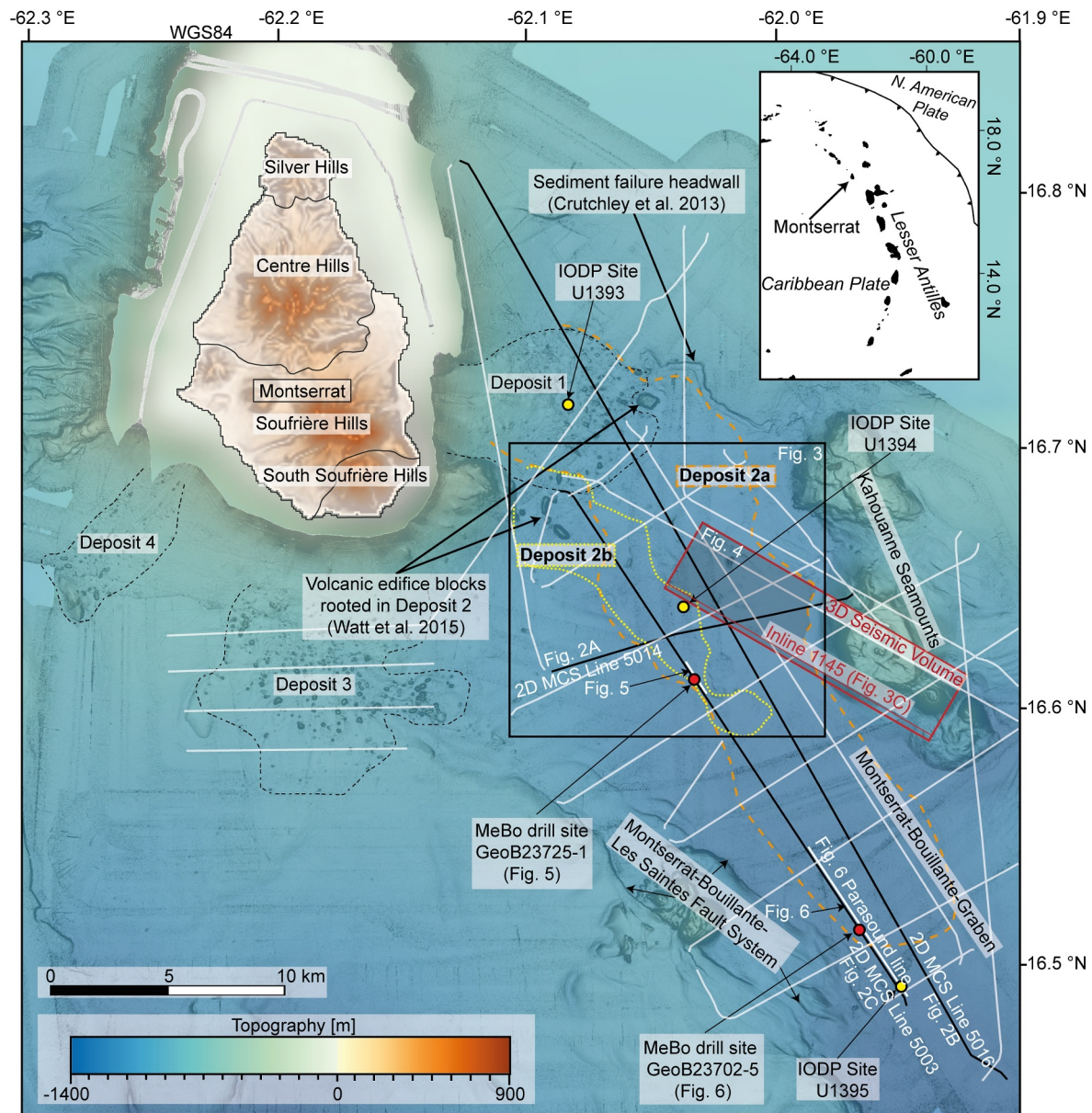
Figure 1. Overview map of the survey area offshore Montserrat. The inset shows the location of Montserrat on the Lesser Antilles Arc. The main map shows Montserrat (SRTM topography) and the newly acquired high-resolution bathymetry data merged with a global GMRT grid (Ryan et al., 2009). The outlines of Deposits 2a and 2b are derived from our new seismic interpretation. White lines mark the newly acquired 2D seismic data and black lines mark the 2D seismic lines shown in Figure 2. The red rectangle outlines the newly acquired 3D seismic volume.

(Karstens et al., 2013; Le Friant et al., 2009; Trofimovs et al., 2008). One of the most intensively studied mass transport deposits is Deposit 2 (Coussens et al., 2016; Crutchley et al., 2013; Hornbach et al., 2015; Le Friant et al., 2004; Lebas et al., 2011; Watt, Talling, Vardy, Heller, et al., 2012, Watt, Talling, Vardy, Masson, et al., 2012). Deposit 2 is an elongated deposit located east and SE of Montserrat broadly following the slope of the M-B-Graben over an extent of roughly 30 km (Le Friant et al., 2004; Lebas et al., 2011; Watt, Talling, Vardy, Masson, et al., 2012) covering an area of ~200 km^2 (Watt, Talling, Vardy, Heller, et al., 2012). The deposit extends from east of the Soufrière Hills onshore to a broad chute in the submerged island flank. Volume estimates for Deposit 2 in previous studies vary between 8.4 km^3 (Lebas et al., 2011) and 9.5 km³ (Watt, Talling, Vardy, Masson, et al., 2012). Deposit 2 is divided into two subunits, Deposit 2a and Deposit 2b, by a package of continuous reflections in seismic data that can be traced over a distance of more than 15 km (Lebas et al., 2011).

The central part of the deposit has a hummocky morphology, while the more distal part is rather smooth surfaced (Watt, Talling, Vardy, Masson, et al., 2012). Crutchley et al. (2013) demonstrated (using 3D seismic data) that the headwall scarp that limits the northern extent of Deposit 2 (Figure 1) was formed by a seafloor sediment failure that was caused by the emplacement of Deposit 2 and incorporated into the main slide mass associated with the deposit. Le Friant et al. (2004) suggested a collapse of the Soufrière Hills volcano as the potential origin of Deposit 2. Remotely Operated Vehicle (ROV) sampling and imagery confirmed that some of the steep-sided polygonal hummocks in the proximal part of Deposit 2, visible in bathymetry and seismic profiles, represent intact fragments of volcanic edifice material (Watt et al., 2015). Deposit 2 and the surficial sub-circular Deposit 1 were targets of an International Ocean Discovery Program (IODP) drilling campaign in 2012 (Expedition 340 Scientists, 2013). During this campaign, only a few meters of volcaniclastic material from Deposit 1 were recovered (Site U1393; Le Friant et al., 2015). Deposit 2 core material included a horizontally stratified and visually undisturbed sedimentary sequence within Deposit 2 (Site U1394; Le Friant et al., 2015), implying that the deposit contains incorporated units of intact seafloor material, alongside turbidite deposits that have been correlated with Deposit 2 based on thickness and stratigraphic relationships, beyond the southern limit of the deposit (Site U1395, Coussens et al., 2016).

3. Methods and Data

During cruise M154-1 aboard R/V METEOR in April 2019 we acquired 2D multichannel seismic data (Berndt et al., 2019; Kühn et al., 2023a), a 3D seismic volume (Berndt et al., 2019; Kühn et al., 2023b), Parasound echosounder data, and multibeam bathymetry (Berndt et al., 2019, 2021). We collected additional Parasound echosounder data and multibeam bathymetry during M154-2 in April/May 2019, and conducted a drilling campaign with MARUM's MeBo70 seafloor drilling device (Huhn et al., 2019).

We collected 2D multichannel seismic data (Figure 2) mainly with an 87.5 m-long (65 channels) active streamer system with a group spacing of 1.56 m and a 3.3 × 13 km 3D seismic data volume (Figure 3, Figure 4) with a P-Cable system. The acquisition geometry of the 3D seismic survey consisted of 14–16 12.5 m-long active sections with a group spacing of 1.54 m attached to a cross cable dragged perpendicular to the sail line direction with a streamer spacing of ~9 m (Berndt et al., 2019). These nominal streamer configurations changed repeatedly (Berndt et al., 2019). Two GI air guns (105/105 cubic inch) fired every 5 s as a seismic source. Before the seismic processing, we applied geometry corrections to the 3D seismic data based on direct wave first arrivals. A malfunction of the seismic source is visible over an extent of >10 km on one profile in Figure 3c. Seismic data processing included binning (bin sizes: 1.54 m (2D) and 3.125 (3D)), trace editing, high-pass filtering (25 Hz cut and 55 Hz slope corner frequencies), denoising (anomalous amplitude attenuation, random noise attenuation, multiple attenuation by adaptively subtracting a multiple model obtained by time-shifting the original traces to the multiple arrival time), predictive deconvolution (to remove bubble noise), normal moveout correction (with 1,511 m/s constant velocity model), stacking, post-stack trace interpolation to infill empty bins (3D only), and finite-difference migration. The velocity model for the migration was built with a velocity of 1,511 m/s in the water column and a gradually increasing velocity of 1,580 m/s at the seafloor reflection to 1,725 m/s at the end of the traces). These velocities were adapted from an Ocean Bottom Seismometer (OBS) experiment during M154-1 (Kunde, 2020) by reducing the OBS velocities until diffraction hyperbola were successfully collapsed to their apices during migration. The vertical resolution of data is ~4 m (one quarter of the dominant wavelength, with a dominant frequency of ~100 Hz and a seismic velocity of 1,580 m/s at the seafloor). Given the binning at 3.125 m (3D) and 1.54 m (2D), the horizontal resolution varies from 1.5 to 5 m from the seafloor to the lower boundary of imaging assuming an increase of migration velocity uncertainty with depth.

Multibeam bathymetry was acquired with a shipboard EM122 multibeam echosounder and gridded with a cell size of 10 m (Huhn et al., 2019). Parasound data were acquired parallel to the acquisition of 2D seismic lines with a dominant secondary frequency of 4 kHz and vertical resolution between 15 cm and 2% of the water depth (range provided by manufacturer). More detailed information on Parasound and multibeam bathymetry acquisition can be found in Berndt et al. (2019) and Huhn et al. (2019). See supporting information for uninterpreted data.

Volumes, vertical separations, and thicknesses of mass transport deposits and sediments in their vicinity were calculated with a seismic velocity of 1,700 m/s derived from the OBS experiment (Kunde, 2020) consistent with
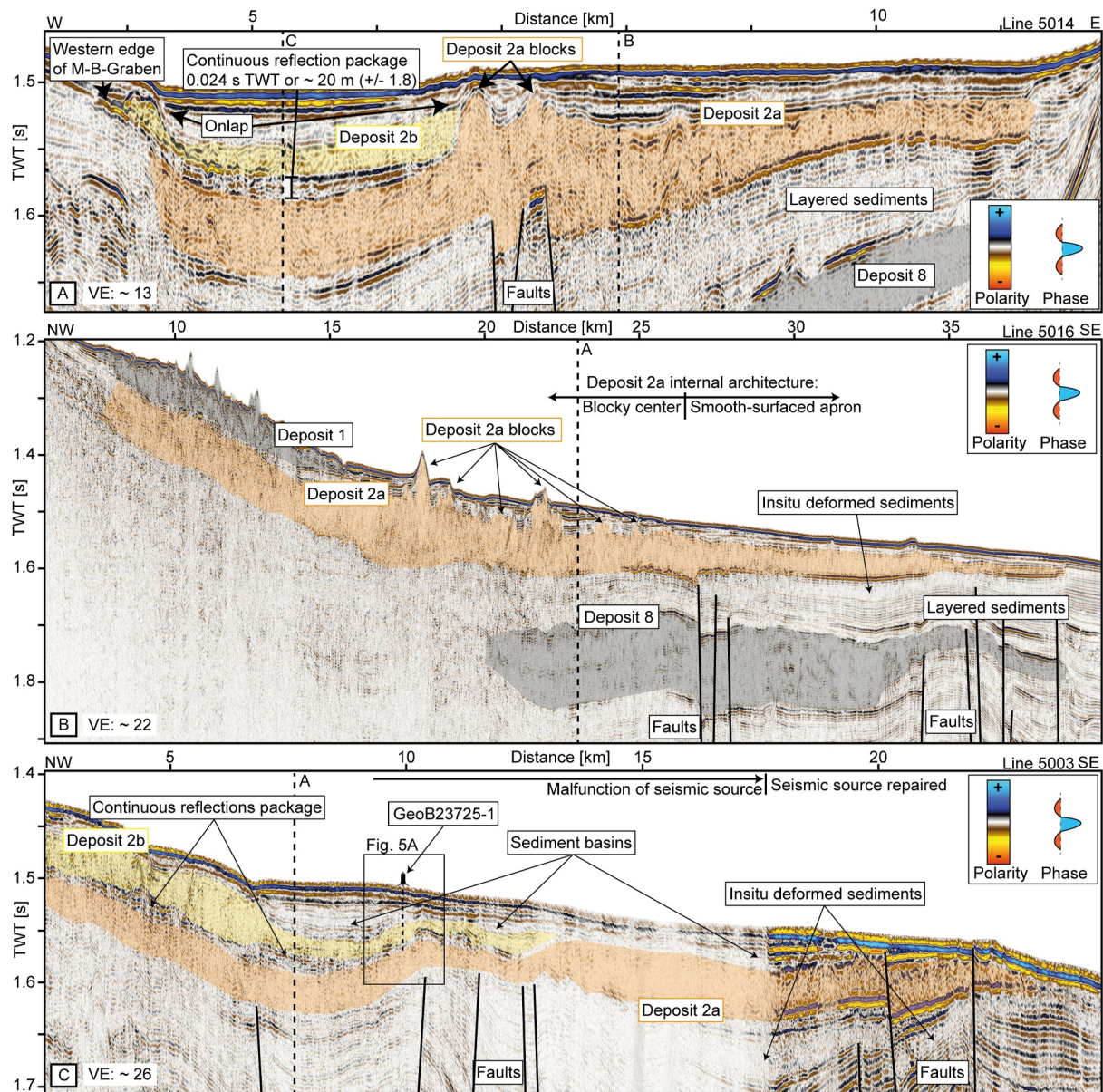
Figure 2. Newly acquired 2D multichannel seismic profiles. (a) Seismic profile 5014 crossing the M-B-Graben and Deposit 2. Deposit 2a (orange) has a blocky center but smoother-surfaced apron west and east of the central blocks. The bottom boundary of the central part is affected by a series of extensional faults. A package of continuous reflections separates 2a and 2b (yellow). The blocks in Deposit 2a and the western edge of the M-B graben form a topographic depression where Deposit 2b is located. (b) Seismic profile along the M-B-Graben. In the proximal domain, Deposit 2a is overlain and overprinted (and likely partly eroded) by Deposit 1. In the center, Deposit 2 blocks breach the seafloor. Downslope of the blocks, the surface of Deposit 2 is smooth, while the amplitude of the base reflection is generally increasing with distance. (c) Seismic profile cutting Deposit 2b and the western edge of Deposit 2a. The continuous reflections between both deposits extend more than 12 km. The morphology is strongly controlled by normal faults within the graben that offset and cut Deposit 2. Topographic depressions above both slide deposits show continuous seismic reflections consistent with the stratified seismic facies.

seismic velocities measured during IODP Expedition 340 of 1,650–1,800 m/s obtained from volcanic layers and 1,550 to 1,650 obtained from background sediments (Le Friant et al., 2015). These velocity ranges indicate a numerical error of +/-9% of our calculated volumes, separations, and thicknesses. We used the same velocity for the integration of core observations and acoustic data. The most proximal portion of the deposits is not imaged with geophysical data. This implies that the stated volumes are minimum volumes. Based on the overall
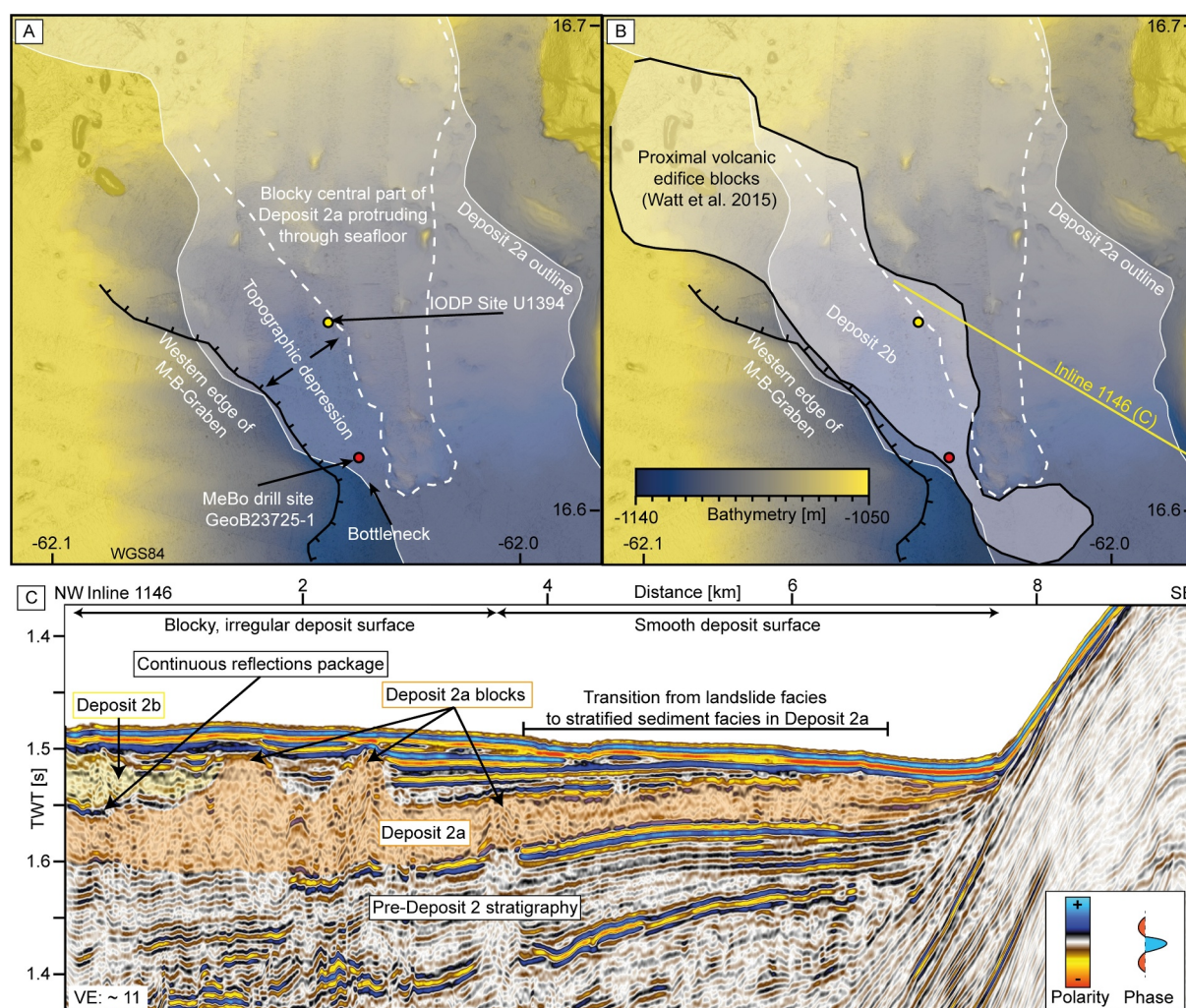
Figure 3. Morphology of the central Deposit 2. (a) The blocky center of the Deposit 2a is clearly elevated from the adjacent sediments and forms an elongated chute with the western edge of the M-B-graben. (b) The outline of Deposit 2b shows that it was deposited in the chute described in (a) Once the associated slide passed the bottleneck at the most distal block accumulation it was emplaced in a sub-circular shape. (c) Inline 1,146 from the 3D seismic volume revealing the internal seismic architecture of Deposit 2.

configuration of the slope stratigraphy with the deposits pinching out toward Montserrat and being more constricted on the upper slope, we assess that the missing volumes are small, that is, less than 0.5 km³. However, the proximal part of Deposit 2 suffers from lower imaging quality as seismic imaging is affected by the overlying Deposit 1. The similarity map shown in Figure 4b was calculated using the Kingdom software with a temporal window length of 0.005 s. The similarity attribute analyses how similar a seismic trace looks compared to its neighboring traces and is widely used in seismic interpretation for the analysis of discontinuities in seismic reflections (Chopra & Marfurt, 2008). Here, similarity was calculated for the whole 3D seismic volume and similarity values were then extracted along the top boundary horizon of Deposit 2a. Volumes and extents outside the 3D seismic volume result from interpolation of the picked horizons between 2D seismic profiles.

We used the seafloor drill rig MARUM-MeBo70 to retrieve sediment core samples of the stratigraphy offshore Montserrat, especially the mass transport deposit referred to as Deposit 2. Freudenthal and Wefer (2013) provided a detailed description of the MeBo70 system. This system recovered 55 mm diameter core samples with a wireline coring technique and a stroke length per core barrel of 2.5 m. We drilled two holes into Deposit 2 at two different locations: GeoB23725-1 in the central part and GeoB23702-5 in the distal part of the slide deposit
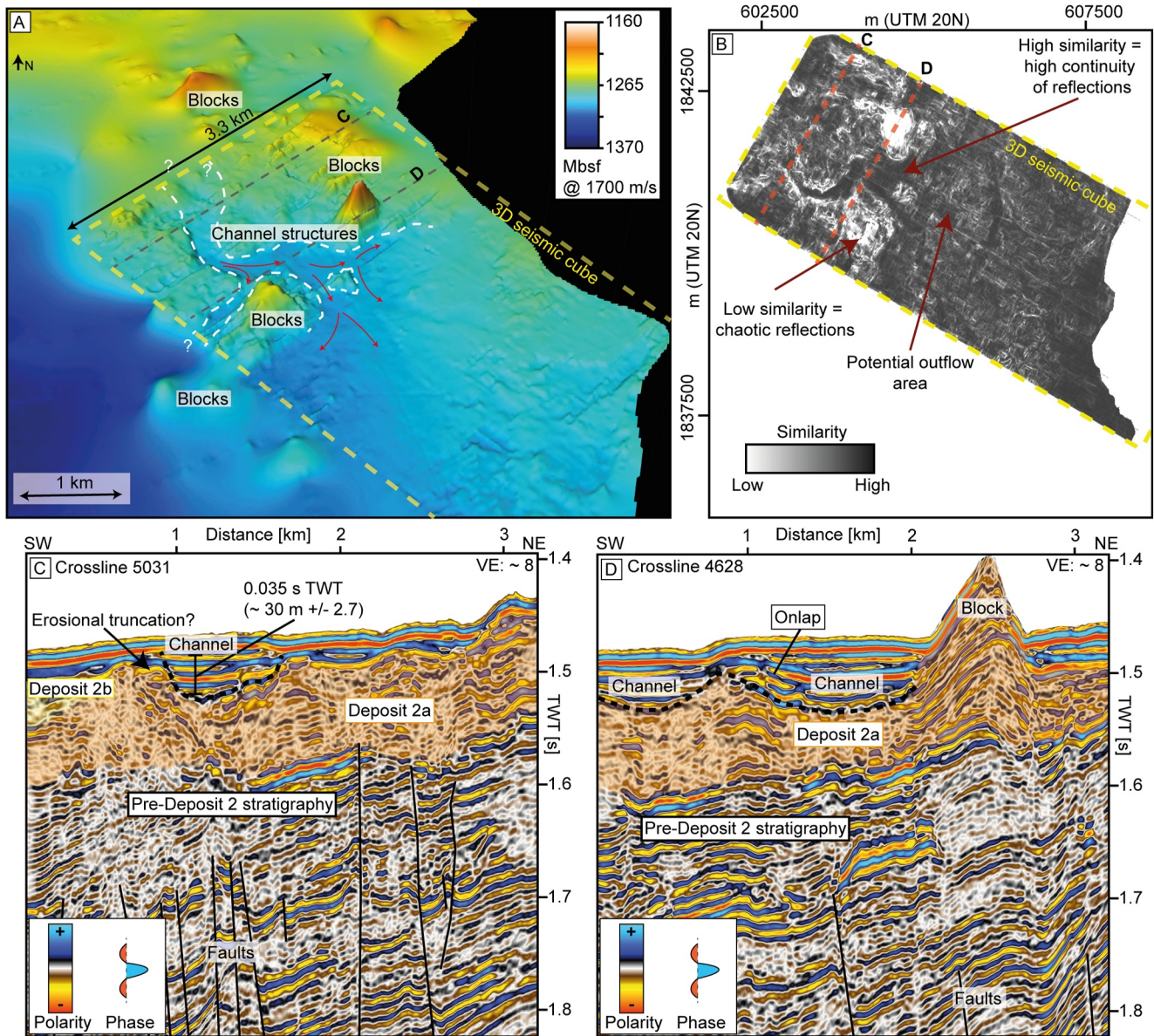
Figure 4. 3D seismic analysis of the top surface of Deposit 2a. (a) 3D surface of Deposit 2a reveals channel structures incised on top of the deposit (black lines). Depths were calculated with a constant velocity of 1,700 m/s. (b) Similarity map of Deposit 2a's surface extracted from the 3D seismic volume. (c) Crossline 5031 from 3D seismic volume showing Deposit 2a (orange), the eastern edge of Deposit 2b (yellow) and the 30 m deep channel incised into the blocky center of Deposit 2a. (d) Crossline 4628 from 3D seismic volume showing Deposit 2a (orange) and two shallower channels incised into it.

(Figure 1). As expected from Expedition 340 (Le Friant et al., 2015), coarse-grained sandy sediments were hard to drill and intruded into the borehole frequently. For this reason, large parts of the drill length were washed and 17 m of core were retrieved in total (Huhn et al., 2019). Drilling depth is given in meters below the seafloor (mbsf). Core parameters and recoveries are given in Table 1.

Table 1
MeBo70 Drill Sites Included in This Study

Drill site	Latitude	Longitude	Drill depth (mbsf)	Coring length (mbsf)	Recovery (m)	Recovery (%)
GeoB23702-5	16°30.883′ N	−61°58.038′ W	30.30	25.71	14.62	57
GeoB23725-1	16°36.728′ N	−62°02.032′ W	41.00	4.00	1.92	48

4. Results

4.1. Seismic and Hydroacoustic Data

4.1.1. Seismic Configuration

In the seismic data set from offshore Montserrat, we interpret two distinct seismic facies consistent with the seismic facies definitions and descriptions in Lebas et al. (2011) and Watt, Talling, Vardy, Masson, et al. (2012). The main seismic facies consists of lateral continuous and coherent, mostly (sub-) parallel seismic reflections with generally consistent amplitudes along the reflection's spatial extent. This seismic facies likely represents stratified and layered sediments. In the following section, we refer to this seismic facies as stratified sediment facies. The second seismic facies comprises partly chaotic, discontinuous, and relatively transparent (i.e., low amplitude) reflections. The top and bottom reflections of this seismic facies are generally of higher amplitude and coherency than the chaotic internal reflections. This seismic facies represents mass transport/landslide deposits and in the following we refer to it as a landslide facies. The internal structures of Deposit 2 and the outlines of Deposit 2a and 2b have been refined here, with the differences from prior interpretations explained in Section 5.1.

The seismic data presented here provide insight into the shallow (upper ∼500 m) stratigraphy of the M-B-Graben with the stratified sediment facies repeatedly interrupted by and interbedded with the landslide facies in discrete horizontal packages of variable extent and thickness (Figures 2a–2c, 3c, 4c, 4d, and 5a). The surfaces of the landslide facies units are partly hummocky in their centers (e.g., Figures 2a and 2b) and partly flat and coherent around these centers (Figures 2a–2c, 3c, 4c, and 4d). Correlation of the landslide facies units with interpretations from earlier studies that used different data sets (Le Friant et al., 2004; Lebas et al., 2011; Watt, Talling, Vardy, Masson, et al., 2012) allows an attribution to the Deposits 1, 2a, 2b and 8. Lebas et al. (2011) provide overview maps of legacy seismic data collected offshore Montserrat, defining these various deposits. In the following section, we address specific landslide facies units within these previously established deposits. Our analysis is focused on Deposit 2a and Deposit 2b.

Extensional faults cut through the stratigraphy and offset entire sediment bodies (e.g., Deposit 8, Figure 2b) and appear to influence the basal surface topography of more recent events (e.g., Deposit 2a, Figure 2b). Topographic depressions formed by faulting or between hummocks are infilled with the stratified sediment facies with onlapping reflections (e.g., Figure 2a).

4.1.2. Deposit 2a

The internal seismic character of Deposit 2a is generally defined by the landslide facies. The deposit has an elongated shape and covers an area of 183 km^2 with a volume 8.9 km^3 (±0.4). The thickness of the deposit is variable, with the greatest thickness of more than 180 m (±16) at the deposit's center, a median thickness of 43 m (±2), thinning out in the most distal part and at the deposit's sides. The northern limit of Deposit 2a is defined by a sediment failure headwall (Figure 1), where the truncation of seafloor strata has been previously interpreted to reflect sediment failure that occurred concurrent with volcanic flank collapse emplacement (Crutchley et al., 2013; Watt, Talling, Vardy, Heller, et al., 2012, Watt, Talling, Vardy, Masson, et al., 2012).

The chaotic internal seismic character of Deposit 2a is broadly consistent over its extent. However, the morphology of the surface can be used to gain insight into its internal architecture. Based on the morphology we divide it into two structural domains: A V-shaped blocky center that is characterized by up to 180 m (±9) high blocks protruding through the seafloor (Figures 2b and 4d), with an irregular rough surface that is elevated from its surroundings by several tens of meters, with sharp lateral margins defining a shape that narrows toward the SE (Figure 3a). This blocky center (outlined in Figure 3a) has a volume of 5.2 km^3 (±0.3). The surface of this blocky deposit, examined in detail using the new 3D seismic volume, reveals features not previously resolvable in the mass transport deposits offshore Montserrat. The images reveal a complex system of 100- to 1,000-m wide channels incised into the top of the blocky surface, with a NW to SE direction in the 3D seismic volume, and with a consistent gradient to the SE (Figure 4). A main channel opens up into three radially distributed sub-channels widening toward the marginal part of the system, coinciding with the limits of the blocky deposit. The observable length of the individual sub-channels combined with the main channel is 2.5–3 km (Figure 4a). Since the extent of imaging of the main channel is limited in the NW by the extent of the 3D seismic volume, the channel system may be sourced from more proximal parts of the blocky deposit, but this area is only covered by sparsely spaced 2D seismic profiles, where the extent of the channel system cannot be tracked due to the more limited spatial
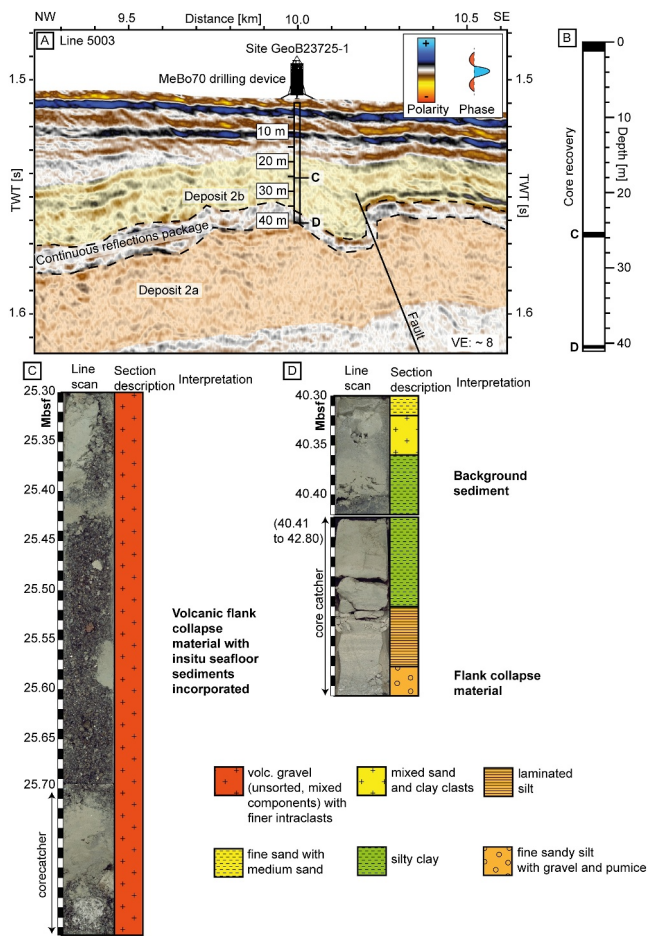
Figure 5. (a) Seismic line 5003 cutting the Deposit 2a-/2b sequence from NW to SE with the location of the MeBo drill site GeoB23725-1. (b) Core recovery at the drill site. White intervals indicate no core recovery. The topmost coring interval is not presented in this study. (c) Core photography alongside stratigraphic logs and facies interpretation. Deposit 2b comprises volcanic flank collapse material with in situ incorporated seafloor sediments, the continuous reflection unit comprises background sediments. Deposit 2a could not be penetrated at this drill site.

coverage. Beyond the blocky central part of Deposit 2a, the channels appear to have an outflow to the SE (Figure 4b) into a portion of the deposit with a smoother surface: the second structural domain of Deposit 2a. We observe reflections characterized by the stratified sediment facies within the channels (Figures 4b and 4d). This infill is limited to the channels without any indications of a drape over the channel margins, with a maximum thickness of up to 30 m ($\pm$1.5) in the northwesternmost part of the main channel.

The smooth surfaced domain of Deposit 2a, which extends as an apron around the southern limits of the blocky central domain (Figures 3 and 4), has a volume of 3.7 km^3 ($\pm$0.2). In the 2D seismic data, this domain is generally defined by the landslide facies. In the Parasound echosounder data, most of Deposit 2a is transparent and no internal reflections are visible (Figure 6a). However, the 3D seismic data show a transition of the landslide facies to a more transparent (i.e., low amplitude) sub-facies of the stratified sediment facies toward SE (Figure 3c).

4.1.3. Deposit 2b

The relief of the blocky center of Deposit 2a and the western edge of the M-B-Graben form an approximately 3-km-wide elongated topographic depression (Figures 2a and 3), which was infilled by Deposit 2b. The internal seismic character of Deposit 2b is represented by the landslide facies. Deposit 2b covers an area of ~37 km^2 (Figure 3b) with a volume of 1.0 km^3 ($\pm$0.05). The deposit's shape is generally elongated (Figure 3b), up to 4.5 km wide closer to Montserrat and gradually narrowing toward its distal margin. Where the most distal blocks of Deposit 2a and the western edge of the M-B-Graben form a bottleneck (Figure 3b), Deposit 2b is only 0.4 km wide, but the deposit radiates south of this bottleneck in a 2.4 km wide sub-circular shape (Figure 3b). The thickness of Deposit 2b gradually decreases from a 30 m ($\pm$1.5) median in its proximal parts to a 20 m ($\pm$1) median at the deposit's toe. The morphology of the proximal Deposit 2b is shaped by a field of up to 800 m wide and up to 180 m ($\pm$16.2) high blocks protruding through the present seafloor. Beyond the proximal blocks, the deposit has a slightly hummocky surface that contrasts with the smooth surface of the Deposit 2a apron (Figures 3a and 3b). Some seismic reflectivity in Deposit 2a (Figure 2b) may be interpreted as the boundary between Deposit 2a and a younger deposit. However, this is not consistent with the boundary being part of Deposit 2b, because the overall shape of Deposit 2b indicates a transport pathway farther west, and we propose that the associated slide bypassed this area.

4.1.4. Continuous Reflections Package

The continuous reflections package that defines the separation of Deposits 2a and 2b in the western parts of Deposit 2 (Watt, Talling, Vardy, Heller, et al., 2012) has a seismic character defined by the stratified sediment facies. This unit is up to 20 m ($\pm$1) thick. We picked the seismic reflections from a distance of 6 km away from the southeastern shore of Montserrat up to a distance of 13 km in the southeastern direction (Figures 2a and c). The shape of the reflection package broadly corresponds to the elongated shape of Deposit 2b. This unit is limited to the topographic depression formed by the edge of the M-B-Graben to the SE and by the blocks of the central Deposit 2a to the east.

4.2. MeBo Drill Core Results

In order to constrain the lithologies within and around Deposit 2, we draw on MeBo drilling at a proximal site, where Deposit 2b, the continuous reflections package and Deposit 2a overlap (GeoB23725-1), ~3 km south of Site U1394, and at a site in the distal part of Deposit 2a (GeoB23702-5), ~3 km NW of Site U1395. The retrieved
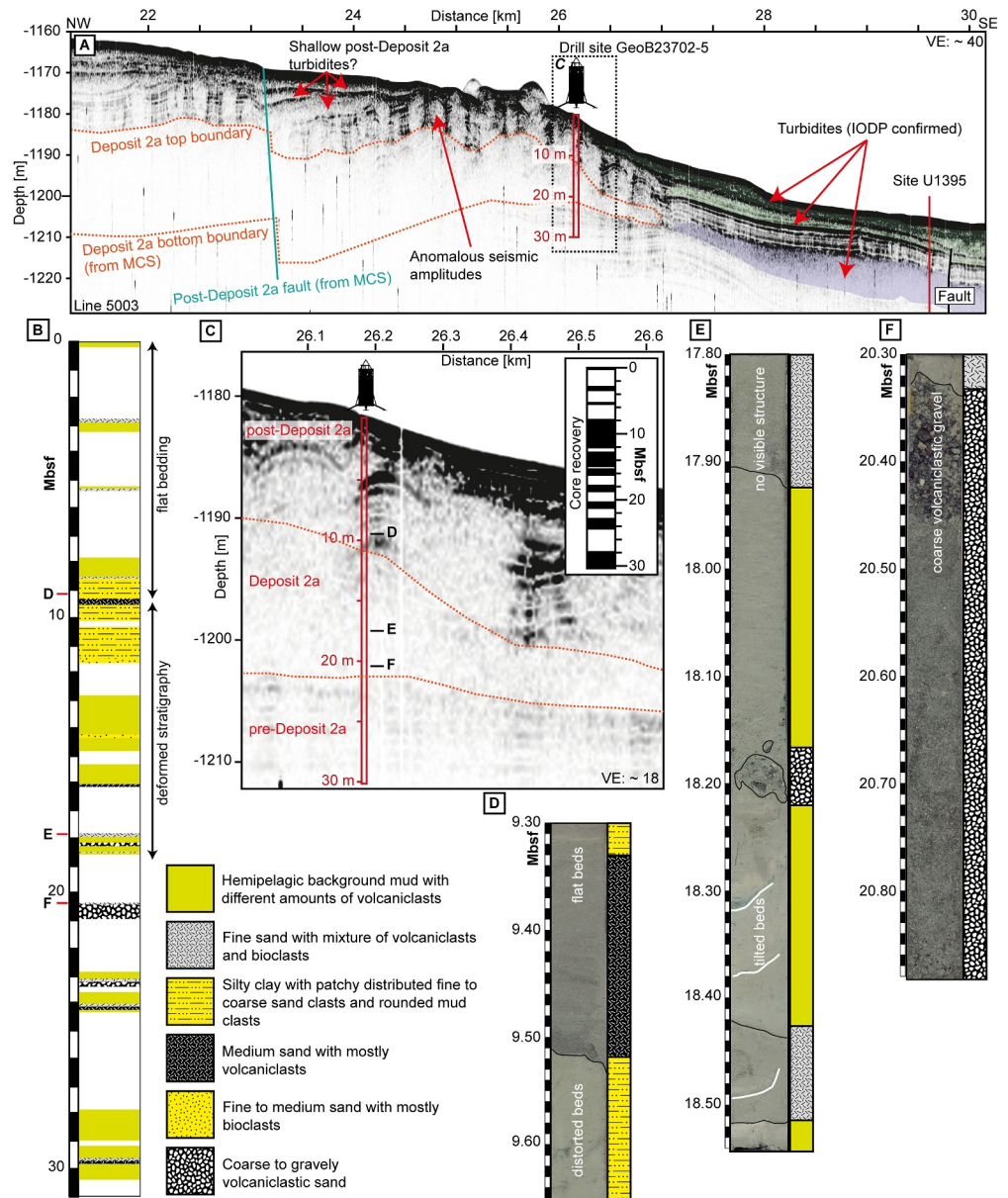
Figure 6. (a) Parasound echosounder profile parallel to 2D MCS line 5003 with the MeBo drill site GeoB23702-5 location. Most parts of Deposit 2a are acoustically transparent in the echosounder, except the southeasternmost km showing deformed stratigraphy with flat lying stratigraphy below the deposit's bottom boundary. (b) Stratigraphic log for drill site GeoB23702-5. (c) Zoomed snippet of (a) Internal stratification within Deposit 2a is visible. Inset: Core recovery. White intervals indicate no core recovery. D-F: Core photography alongside corresponding stratigraphic logs.

cores provide insight into the lithological composition of the Deposit 2 subunits and add to the interpretation of processes that led to the seismic characteristics described in the previous subsection.

4.2.1. GeoB23725-1 Drill Core Results

GeoB23725-1 (Figure 5) was drilled at a water depth of 1,127 m in a topographic depression between the blocky center of Deposit 2a and the western edge of the M-B-Graben ~15 km SE of Montserrat. Drilling was conducted to a depth of 41 mbsf (Table 1). With the overarching aim to sample different sections of Deposit 2, large parts were flushed down without intentional coring to avoid the drill tool getting stuck in the coarse and heterogeneous sediment at this site. A seafloor section from 0 to 1.07 mbsf was located above (seismically defined) Deposit 2b

and we do not further analyze it in this study. The other recovered material was from two short sections, which provide insights into the internal composition of Deposit 2b, from 25.30 to 25.85 mbsf (including core catcher) (Figure 5c), and the continuous reflections package from 40.30 to 40.58 mbsf (including core catcher) (Figure 5d). Core recovery was 48% in these sections. The core interval from 25.30 to 25.85 mbsf was located within Deposit 2b (Figure 5a) and comprises mixed-component volcanic gravels with cm-sized silt and sand intraclasts, and pumice intraclasts in the lowermost 2 cm (Figure 5c). Although core recovery from Deposit 2b within the prior IODP cores at Site U1394 was extremely low, isolated sections recovered in the core catcher retrieved volcanic clasts, sand and hemipelagic mud (Coussens et al., 2016). Based on our observations of mixed marine sediment intraclasts within volcaniclastic gravels, the recovered material from Site U1394 is consistent with our new observations of Deposit 2b. The bottommost core interval from 40.30 to 40.58 mbsf was located at the base of the continuous reflection package separating the seismic units of Deposit 2b and Deposit 2a (Figure 5d). This interval comprises fine to medium sand, mixed sand and clay clasts, silty clay and laminated silts. The lowermost 2 cm of the core catcher material comprises fine sandy silt with volcanic gravel and pumice. Coring of the continuous reflections package was not previously successful during IODP drilling of the equivalent section at Site U1394, although the underlying Deposit 2a had good recovery, comprising hemipelagic muds interbedded with compositionally varied turbidites (Coussens et al., 2016; Le Friant et al., 2015), indicating that Deposit 2a at this location was comprised of the local marine stratigraphy.

4.2.2. GeoB23702-5 Drill Core Results

GeoB23702-5 (Figure 6) was drilled ∼27 km SE of Montserrat at a water depth of 1,170 m to a depth of 30.30 mbsf (Table 1). Sections retrieved from a depth of 0–3.24 mbsf comprise flat-lying hemipelagic mud with frequent thin, horizontal volcaniclastic medium to fine sands, interbedded with mixed volcaniclastic and bioclastic sands, silty clay layers, and discontinuous sand and mud patches (Figure 6b). This is consistent with the lithologies found in the shallowest sections at the previously drilled IODP Site U1395 (Coussens et al., 2016). From 5.30 to 9.40 mbsf, GeoB23702-5 comprises flat-lying hemipelagic mud overlying mixed volcaniclastic and bioclastic sands and silty clay layers, with patchy sands and rounded mud clasts. Although this is generally consistent with the hemipelagic mud-dominated lithology found at Hole U1395 B, core recovery with MeBo was very low within the upper 10 mbsf (Figure 6c, inset) and we do not observe several of the shallow turbidites described in Coussens et al. (2016) and Le Friant et al. (2015) due to this poor recovery. The correlation between the Parasound line 5003 and GeoB23702-5 (Figure 6) allows us to identify the position of Deposit 2a within 9.4–21 mbsf, where we observe a sharp transition from horizontal beds to deformed beds (Figure 6d), within a similar set of lithologies to the overlying beds. The deformation is evident as distorted beds and structureless sections (with similar color, grain-size and compositional characteristics to the upper stratigraphy), and as tilted beds in the central part of this section (Figure 6e). Comparable deformation in the distal part of a mass transport deposit was observed at Sites U1399 and U1400 offshore Martinique, where tilted beds broadly correspond to thrust and fold structures in seismic data (Brunet et al., 2016), within the outer parts of a large mass transport deposit comparable in overall form to Deposit 2. The lower part of Deposit 2a in GeoB23702-5 contains distorted and folded beds with pods of volcaniclastic gravel and sand. In its lowermost interval, it contains a ∼50 cm thick layer of volcaniclastic coarse sand grading up into an upper layer of volcaniclastic gravel, at a depth of 20.30–20.89 m (Figure 6f). The pre-Deposit 2a stratigraphy contains mostly hemipelagic background mud with a variety of thin flat lying beds similar in character to those of the sediment above Deposit 2: volcaniclastic sands, and beds of fine sand with a mixture of volcaniclastics and bioclasts. The pre-Deposit 2a unit at ∼24 m (Figure 6b) is distinctive in being coarse grained and pumice rich, contrasting with the dark volcaniclastic sands and gravels that are dominant offshore Montserrat (cf. Trofimovs et al., 2013). This unit is consistent with the stratigraphic sequence in the previously drilled IODP Hole U1395 B (Coussens et al., 2016), supporting a correlation between the two sites (Figure 6). In Hole U1395 B, the next volcaniclastic horizon above the pumice is a dark volcaniclastic coarse sand to gravel, which we correlate with the coarse sand at the base of Deposit 2a at site GeoB23703-5 (as defined in Figure 6). In Hole U1395 B, this is separated by ∼25 cm of hemipelagite from an overlying very thick turbidite containing volcaniclastic sands and gravels, with deformed hemipelagite and multiple graded units (best recovered in Hole U1395 A), and spanning ∼8 m. This very thick turbidite is clearly imaged in our Parasound data (Figure 6a) with a thickness and stratigraphic position consistent with the core stratigraphy at Site U1395. Taken together, these observations suggest that the coarse volcaniclastic sand to gravel that defines the base of Deposit 2 at GeoB23703-5 represents a discrete high-energy event that preceded Deposit 2 emplacement.

Table 2
Deposit 2 Characteristics in Literature and in This Study

Reference	Area (km^2)	Runout (km)	Thickness (m)	Volume (km^3)	Age (ka)
Le Friant et al., 2004	200 (total)	30 (total)	40–50 (total)	-	112–130
Lebas et al., 2011	190 (total)	30 (total)	58–64 (total)	8.4–9.2 (total)	~233
Watt, Talling, Vardy, Masson, et al., 2012	212 (total)	23 (Deposit 2a)	45 (total)	9.5–10.3 (total)	~140
	84 (Deposit 2a)	34 (Deposit 2b)	39 (Deposit 2a)	3.2–3.5 (Deposit 2a)	
	181 (Deposit 2b)		35 (Deposit 2b)	6.3–6.8 (Deposit 2b)	
Le Friant et al., 2015	-	-	-	-	138 (Deposit 2; Deposit 2b in this study)
This study	183 km^2 (Deposit 2a)	32 (Deposit 2a)	~43 (Deposit 2a)	9.9 (total)	~318 (Deposit 2a)[a]
	37 km^2 (Deposit 2b)	15 (Deposit 2b)	~30 (Deposit 2b)	8.9 (Deposit 2a)	
				1.1 (Deposit 2b)	

[a]Based on the age dating of Deposit 2b in Le Friant et al. (2015).

5. Discussion

5.1. Volume and Shape Differences in Respect to Previous Studies

Volume, vertical distance, and thickness calculations require the conversion of seismic TWT to depth involving specific seismic velocities. For this study, we used a constant seismic velocity of 1,700 m/s (Kunde, 2020), which was derived from an OBS experiment that targeted Deposit 2. The value is within the range of velocities measured during Expedition 340 between 1,550 m/s minimum for hemipelagic background sediments and 1,800 m/s maximum for volcanic deposits (Le Friant et al., 2015). The uncertainty in this conversion velocity implies an uncertainty of the calculated vertical distances of ±9%. Given the fact that the MeBo cores presented here (e.g., Figure 4c) and also the cores from IODP Expedition 340 (e.g., Le Friant et al., 2015) and the new OBS data provide a consistent velocity range, and because of the interlayering of background sediments with volcaniclastic turbidites and mobilized clasts of background sediments within volcaniclastic units, it is prudent to use this average value for all depth conversions. The new volumes presented in this study are therefore more robust than previous estimations for which no independent seismic velocity information was available. This has to be taken into account when comparing the new volumes with previously published results. In addition to the uncertainty from the seismic velocity, there are some uncertainties and error sources that are less quantifiable: (a) Large parts of the volumes and thicknesses were calculated with seismic horizons that were interpolated between 2D seismic lines, sometimes over several kilometers. (b) The derived volumes neglect erosional processes and do not include turbidites beyond the data resolution or data limits creating a bias toward smaller volumes. (c) There will be subjective choices of the seismic interpreter regarding the identification of horizons (Clare et al., 2019), but the new denser data reduce these uncertainties. In spite of these limitations our calculated Deposit 2 volume of 9.9 km^3 (±0.9) is broadly consistent with previous studies (Lebas et al., 2011: 8.4 km^3, Watt, Talling, Vardy, Masson, et al., 2012: 9.5 km^3; Table 2). However, the volumes for the sub-units Deposit 2a (8.9 km^3 ± 0.8) and 2b (1.0 km^3 ± 0.09) are markedly different: Watt, Talling, Vardy, Heller, et al. (2012) attribute a volume of 3.2 km^3 to Deposit 2a and 6.3 km^3 to Deposit 2b (Table 2). This discrepancy with our new results is mostly caused by the increased spatial resolution of the new, closely spaced 2D seismic data as well as the 3D seismic volume from M154-1. These data allow us to trace the continuous reflection package and hence, Deposit 2b in greater detail compared to earlier studies. For completeness, we tied the new interpretations to the previous interpretations based on previously available (expedition JC45) seismic data (Lebas et al., 2011; Watt, Talling, Vardy, Heller, et al., 2012). The 3D seismic volume allows precise reconstruction of the central blocky region of the deposit into the zone of 2D seismic coverage. This leads to a more precise and narrower outline of Deposit 2b, and to the assignment of the eastern and southernmost part of Deposit 2 to Deposit 2a rather than 2b. This assignment has profound implications for the interpretation of the emplacement mechanisms and the sequence of events represented by Deposit 2.

5.2. Multi-Stage Emplacement of Deposits 2a and 2b

Deposit 2b is separated from Deposit 2a by an up to 20 m thick package of broadly continuous parallel reflections. Understanding the nature of this unit is key in reconstructing the emplacement sequence amalgamating in Deposit 2. The MeBo drill core that targeted the continuous reflections package separating Deposits 2a and 2b, at Site GeoB23725-1, recovered fine sand and silt within this depth range (Figure 5). We interpret this fine-grained material as background hemipelagic sediments, and it is typical of the sediment types recovered in offshore stratified sequences elsewhere in the region (e.g., Coussens et al., 2016; Le Friant et al., 2015; Trofimovs et al., 2013). The sediments observed at Site GeoB23725-1 are horizontally layered, well-stratified, undeformed, and broadly undisturbed. Thus, they do not represent failed and remobilized sediments comparable to those that would be expected to derive from the seafloor failure headwall at the northern end of Deposit 2 (Crutchley et al., 2013). This supports the hypothesis that Deposits 2a and 2b were not deposited during one event, and instead, indicates a time gap between them that is large enough for several meters of background sediment to accumulate. Le Friant et al. (2015) correlate mafic deposits overlying Deposit 2 at Site U1394 to the South Soufriere Hills activity on Montserrat, thus obtaining a minimum age of 138 ka for Deposit 2b. The 15 m of sediment that overlies Deposit 2b at Site U1394 allows us to speculate on the age represented by the ∼20 m sediment package that separates Deposits 2a and 2b, assuming a similar rate of accumulation of ∼0.08 m/Kyr. This rate is within the range of sedimentation rates at Site U1395 of 0.02–0.17 m/Kyr based on oxygen isotope stratigraphy (Coussens et al., 2016) and consistent with the mean sedimentation rate of the shallowest sediments at Site U1395 of ∼0.09 m/Kyr Based on magnetostratigraphy (Le Friant et al., 2015). This implies a time span of ∼180 Kyr for the intervening package, and a minimum age estimate for Deposit 2a of 318 ka. This is a minimum because Deposit 2b likely eroded and incorporated the underlying substrate during its emplacement. We also note that any age estimate not derived from absolute age dating methods is associated with large uncertainties mainly caused by the fact that they cannot accurately account for erosional processes and that sedimentation rates derived from sequences rich in turbidite deposits are likely highly variable. The age of 318 ka is older than any dated subaerial rocks from the Soufriere Hills and lies within a time gap between this volcano and the youngest known rocks from Center Hills (0.55 Ma) (Watt, Talling, Vardy, Masson, et al., 2012). The event may therefore represent a part of the Soufriere Hills stratigraphy that is no longer represented in subaerial exposures.

5.2.1. Volcanic Flank Collapse

Our data combined with previous studies (Le Friant et al., 2004; Lebas et al., 2011; Watt, Talling, Vardy, Heller, et al., 2012, Watt, Talling, Vardy, Masson, et al., 2012; Watt et al., 2015) indicate that the formation of Deposits 2a and 2b was initiated by a volcanic flank collapse that originated from the Soufrière Hills volcano on Montserrat (Figure 7a). We observe an accumulation of blocks in the proximal domain of Deposit 2a. Such proximal block accumulations are often observed at volcanic flank collapse deposits, for example, at the Cape Verde islands (Barrett et al., 2020; Day et al., 1999), the Canary Islands (Krastel et al., 2001), or Ritter Island (Karstens et al., 2019; Silver et al., 2009), as well as at the Deposits 1, 3 and 4 offshore Montserrat (Figure 1; Lebas et al., 2011; Watt, Talling, Vardy, Heller, et al., 2012, Watt, Talling, Vardy, Masson, et al., 2012). Often such block fields have a fan-like or sub-circular shape that indicates a freely spreading flow of the associated debris avalanche along the seafloor during emplacement (Yoshida et al., 2012) and a common source of the material, as well as a deposition by one single event (Kühn et al., 2021). Deposit 2a is different: it is elongated and the V-shaped proximal block field extends with a main axis parallel to the graben axis of the M-B-Graben from NW to SE. This indicates a focused transport of the blocks first downslope of the flank of Montserrat in an initially eastward direction followed by a turn of the transport direction by ∼45° along the graben axis following the steepest downslope trend into the graben center. Lebas et al. (2011) suggest a link between the formation of the mass transport deposits offshore Montserrat and the fault systems that form the M-B-Graben. Compared to Deposit 1, that has a fan-shaped distribution of proximal blocks (Crutchley et al., 2013; Le Friant et al., 2004; Lebas et al., 2011; Watt, Talling, Vardy, Heller, et al., 2012), the blocks of Deposit 2a traveled much further. The mechanism behind this increased travel distance remains unclear, although a focus on the kinetic energy of the slide by a narrowing of the slide plane due to the graben morphology might have led to an increased slide velocity and thus a longer runout of the blocks. The channelization of debris flows can also lead to an increased water-saturation at the base of the flow that ultimately results in increased mobility and longer runouts (Tost et al., 2014). Several numerical models of onshore landslides support the idea that channeling of a slide mass can increase the overall runout distance (Fannin & Wise, 2001; Shen et al., 2022). Watt et al. (2015) showed that some
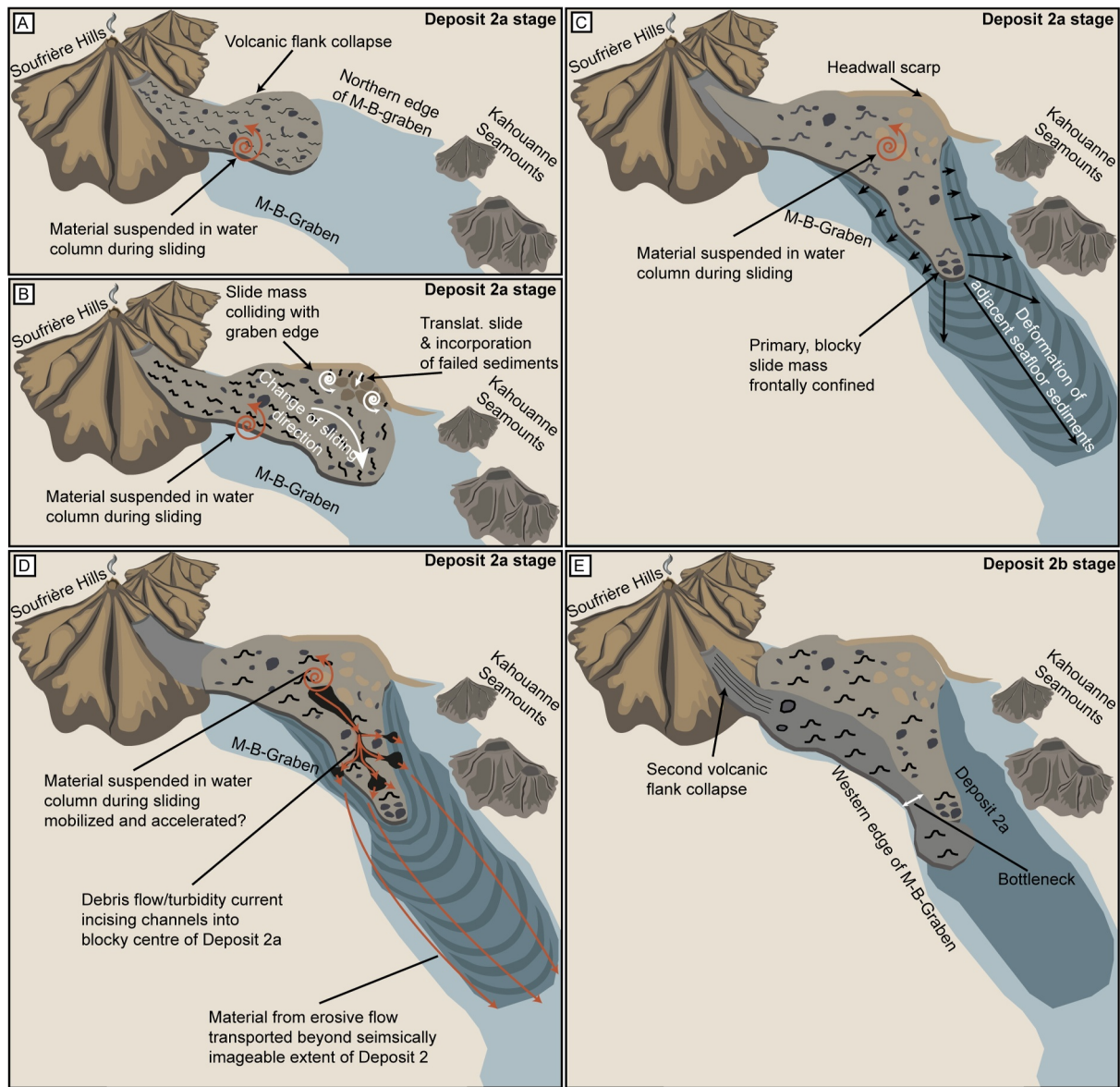
Figure 7. Geological processes involved in the emplacement of Deposit 2 and their assumed timing within the deposition sequence. (a) Initial volcanic debris avalanche from Montserrat. (b) The volcaniclastic slide mass collides with the northern edge of the M-B-Graben and triggers secondary failure of seafloor sediments. (c) The slide mass incises into the substrate and deforms adjacent sediments. Fine grained material is suspended in the water column. (d) Fine grained material suspended in the water column accelerates downslope and forms an erosive flow that incises channel structures into the top surface of Deposit 2a. (e) A second volcanic debris avalanche is emplaced in a topographic chute formed by the Deposit 2a blocks and the western edge of the M-B-Graben.

of the most proximal Deposit 2a blocks are indeed transported volcanic edifice blocks originating from the Soufrière Hills. Therefore, it is likely that the blocky center part of Deposit 2a mainly consists of volcanic flank collapse material, but the secondary seafloor failure at the northern headwall (Crutchley et al., 2013) also contributed to the total volume of this part of the deposit (Figure 7b). The sparse data in the proximal deposition area does not allow a distinction between volcanic material or secondary failed and incorporated seafloor sediments within the blocky center.

The drill cores from site GeoB23725-1, where Deposit 2b overlies Deposit 2a, despite their very limited recovery, suggest that the landslide facies comprises mixed volcaniclastic gravel with hemipelagic background sediment intraclasts. This lithology is consistent with volcanic flank collapse processes forming a debris avalanche that incorporated preexisting seafloor sediment (intraclasts) during emplacement (Figure 7e). The geometry of the

deposit and the proximal accumulation of blocks indicate an origin from the Soufrière Hills on Montserrat (cf. Watt et al., 2015; Figure 1). Similar to the formation of Deposit 2a, the blocky proximal part of Deposit 2b was confined between the prior accumulation of Deposit 2a and the western edge of the M-B-Graben (Figure 3), focusing the flow and producing an elongated geometry rather than a freely spreading deposit. Once the associated slide mass passed the distal bottleneck of this transport pathway (Figure 3b), it was deposited in a sub-circular shape, consistent with unconfined spreading (cf. De Haas et al., 2015). We conclude that the topographic complexity of this volcanic setting, including topography generated by stacked debris avalanche deposits, exerts a strong control on the transport distance and morphology of debris avalanche deposits. Due to the unusual seafloor morphology in volcanic island areas (partly caused by emplaced volcanic landslide deposits), it seems likely that this effect might be widely seen around other volcanic islands.

5.2.2. Sediment Erosion, Incorporation, and Deformation

Beyond the blocky central part of Deposit 2a, the morphology of the bounding surfaces of the deposit is defined by a laterally confined, smooth surfaced apron. The drill cores from the distal site GeoB23702-5 show that this deposit comprises a mixture of deformed, tilted and structureless sediment, lithologically consistent with the hemipelagic basin infill, and with an intermixed volcaniclastic component. The visually deformed and disrupted nature of the sediment comprising Deposit 2a at this site is consistent with the mostly acoustically transparent nature of the deposit in Parasound profiles. Although even small amounts of deformation may have large consequences for the seismic character of a sedimentary unit (Ford et al., 2023; Karstens et al., 2023), the seismic character suggests that the deformation observed in the cores is laterally extensive and may imply disaggregation and loss of structures within the materials mobilized in this part of Deposit 2a (Figure 6). NW/SE oriented seismic profiles show that emplacement of the blocky center and of the smooth-surfaced apron occurred broadly on the same bottom surface, although seismic amplitudes are much higher and more continuous in the apron (Figures 2b and 2c). We suggest that the blocky slide mass that constitutes the center of Deposit 2a incised into the M-B-Graben substrate during emplacement, incorporated pre-existing seafloor sediments and deformed the frontal and adjacent seafloor sediments (Figure 7c). This is broadly consistent with findings from IODP Expedition 340 that recovered hemipelagic mud and turbidites at Site U1394 (Le Friant et al., 2015). Although undeformed, Le Friant et al. (2015) interpret these layers as an intact sediment block within Deposit 2a. Similar deformation of adjacent sediments has been observed in deeper mass transport deposits offshore Montserrat (Deposit 8; Watt, Talling, Vardy, Masson, et al., 2012), Martinique (e.g., Brunet et al., 2016; Le Friant et al., 2015), Israel (Frey-Martínez et al., 2006), Japan (Morita et al., 2011) and Oregon, USA (Lenz et al., 2019). We observe substrate incorporation in the Deposit 2b core sections (background sediment intraclasts) and this process has also been observed elsewhere (Karstens et al., 2019; Kühn et al., 2021; Ogata et al., 2014, 2019; Watt et al., 2019). The volcaniclastic gravel at the base of the distal Deposit 2a apron (Figure 6f) marks the transition of the (seismic) Deposit 2a into the pre-Deposit 2a stratigraphy and was likely deposited in an earlier (pre-Deposit 2a) volcanic flank collapse event. Site U1395 shows a similar volcaniclastic sand-gravel deposit at an equivalent horizon (also stratigraphically constrained by an underlying pumiceous deposit) (between 18 and 20 mbsf; Coussens et al., 2016), causing strong peaks in natural gamma radiation and magnetic susceptibility logging (Expedition 340 Scientists, 2012). We suggest that this volcaniclastic gravel unit potentially acted as a basal shear surface for the deformation of the Deposit 2a apron sediment package (Frey-Martínez et al., 2006; Sobiesak et al., 2018; Watt, Talling, Vardy, Masson, et al., 2012), which would have enhanced the total runout distance and potentially controlled the thickness of the deformed sediment package and incision driven by the Deposit 2a event. However, the data available do not provide clear evidence for this and the nature and age of the older event, depositing the basal volcaniclastic unit in Deposit 2a, is unconstrained. Given its lithology and coarseness, it would be expected to correlate with a proximal volcaniclastic debris avalanche deposit, but this cannot be clearly distinguished in seismic reflection profiles across the proximal sequence offshore Montserrat. Regardless, the sequence points to the occurrence of at least two major mass transport events over several tens of kiloyears, which collectively contributed to the seismically defined Deposit 2.

5.2.3. Suspension of Fine-Grained Flow Material and Channel Formation

Submarine canyons and channels are common morphological features around volcanic islands and an expression of downslope sediment transport by bottom currents usually parallel to the topographic gradient (Casalbore et al., 2021; Hansen et al., 2015; Normark & Carlson, 2003; Shepard, 1981). The channels incised into the top of

Deposit 2a bend around obstacles while broadly being oriented downslope along the axis of the M-B-Graben from NW to SE. The channel system bypasses GeoB23725-1 and Site U1394 and thus does not allow any correlation of specific cored lithologies to a channel forming event. The fact that these channels are incised directly on top of Deposit 2a indicates that they were formed after the main slide event. The lack of meandering and their sharp edges indicate their origin from high energetic, high velocity, erosive flow (Davies & Tinker, 1984).

These observations mimic what has been observed at the top of the Ritter Island sector collapse deposits, where sets of similar channels exist (Karstens et al., 2019; Watt et al., 2019). At Ritter Island, a set of channels formed in the proximal deposit are the result of erosive evacuation of the main collapse material, that then transported most of the sector collapse material into the more distal area of the deposit (Karstens et al., 2019; Watt et al., 2019). This erosion intensified when the flow was focused between two adjacent islands, resulting in an increasing channel depth (Karstens et al., 2019). A second set of channels developed in the distal Ritter Island sector collapse deposits, where a late-stage turbidity current linked to a post-collapse eruption eroded into the distal parts of the initial debris flow deposits (Watt et al., 2019). Due to the lack of drill cores from Deposit 2a, we cannot draw further insights into how directly the channelization observed at Montserrat replicates the processes inferred at Ritter Island, but the fact that the channels are situated topographically higher than Deposit 2b indicates that their formation is not associated with the emplacement of Deposit 2b and that they were rather formed at the end of deposition of Deposit 2a or shortly after.

Trofimovs et al. (2008) reported the transition of pyroclastic flows associated with the 2003 dome collapse of the Soufrière Hills into turbidity currents that transported fine-grained material from the near-shore down the slopes of Montserrat and eroded and incorporated substrate material. The 2022 eruption of Hunga volcano demonstrated that the resulting turbidity currents can travel with velocities up to 33 m/s, run out for long distances (>100 km) and erode substantial amounts of the seafloor (Clare et al., 2023). Water tank experiments on subaqueous landslides also showed that fine grained sediments can be suspended in the water column during sliding (Elverhoi et al., 2010; Mohrig et al., 1998) and there are multiple studies providing evidence for elevated sediment suspension in the water column after earthquake-related turbidity currents (McHugh et al., 2011; Noguchi et al., 2012; Thunell et al., 1999). After the deposition of turbidity currents related to the Tohoku Earthquake in 2011, Noguchi et al., 2012 reported an elevation of suspended sediments in the water column from ~0.6 mg/L to up to 5 mg/L maximum. For the Deposit 2a slide, our data suggest two stages: the primary volcanic flank collapse and the secondary seafloor failure; both could potentially have suspended large amounts of sediment in the water column resulting in a density flow after the main slide mass had already come to rest, and this may be the origin of the post-depositional channelization. Although it is possible that a separate event, undetected within our data, may have incised the channels atop of Deposit 2a, the fact that there are no similar incised channels observed elsewhere in our stratigraphic succession leads us to conclude that the channel and turbidite formation are causally related to Deposit 2a emplacement.

5.2.4. Turbidite Deposition

IODP Expedition 340 reports several (partly) volcaniclastic turbidites at Site U1395 in the M-B-Graben beyond the distal limit of Deposit 2a (Le Friant et al., 2013, 2015). This is consistent with our observation of several near-surface, frontally non-confined, and transparent units in the Parasound echosounder data south of the Deposit 2a toe (Figure 6a) that likely represent turbidite deposits or in situ deformed sediments. Two of these transparent units are located in a depth interval of 0–8 mbsf and are stratigraphically within the corresponding depth interval to Deposit 2a (green-colored units in Figure 6a). Site U1395 cores comprise several cm to m thick turbidites at this depth (Coussens et al., 2016), but due to the limited vertical resolution of the Parasound data, we cannot link single turbidites from the IODP cores to certain transparent units. However, the turbidites are likely related to the formation of the channels on top of the Deposit 2a blocky center as well as potentially to the later deposition of Deposit 2b. A very thick turbidite at Site U1395 (~12–20 mbsf; Coussens et al., 2016) has a stratigraphic depth that corresponds closely with the position of Deposit 2a in our seismic and Parasound profiles (purple-colored units in Figure 6a), and with the deformed sediment of Deposit 2a observed at Site GeoB23702-5. While the stratigraphic position of a distinctive pumiceous horizon at both core sites supports a correlation of this turbidite with Deposit 2a, the lithology found in our MeBo drill cores (mainly background sediment) and the seismic mapping results described in this study rather suggest an earlier (i.e., pre-Deposit 2a) emplacement of this turbidite. Although we favor the latter hypothesis here, more data and analysis are required to infer a correlation of these distal turbidites with Deposit 2a or other mass transport deposits. Shallow transparent units on top of

Deposit 2a (Figure 6a) show similar seismic characteristics as the distal turbidites; therefore, we interpret them as post-Deposit 2a turbidites. This is consistent with the occurrence of shallow, several meters thick turbidites above Deposit 2b at Site U1394 (Le Friant et al., 2015). The relationship between Deposit 2a and the downslope turbidite stratigraphy also depends on whether the distal part of Deposit 2a was frontally confined or unconfined. Parasound profiles suggest a confined mass, but this interpretation remains equivocal based on the available profiles. A complete resolution of turbidite stratigraphic relationships and their correlation with individual landslide events would require geochemical and sedimentological correlations, alongside further geophysical data.

6. Conclusions

Deposit 2 consists of two separate volcanic flank collapse deposits with a significant time gap (∼180 Kyr) in between, great enough for the deposition of ∼20 m of background sediments. In consequence, the bulk volume of Deposit 2 cannot be used for tsunami modeling as it (a) does not account for the origin of material as it neglects any erosional bulking and as it (b) does not account for the individual timing of the at least two discrete volcaniclastic landslides. If these stratigraphic complexities are not resolved, simplified interpretations of debris avalanche deposits offshore volcanic islands overestimate tsunami magnitude. Conversely, the same interpretations may underestimate flank collapse frequency, given that what may initially appear to be a single deposit within bathymetric or low-resolution seismic reflection data sets may actually comprise a series of stacked deposits from discrete events. We suggest that the possibility of multiple stages in the formation of deposits offshore volcanic islands must be considered to produce robust assessments of the tsunamigenic potential of ancient deposits. However, we acknowledge that such assessments remain highly challenging; even with the rare combination of 3D seismic-reflection data sets alongside core sampling and other geophysical data sets, there remain a number of uncertainties in the relative timing and nature of the events that formed Deposit 2 offshore Montserrat.

Our new observations provide a clear illustration of how topography exerts a crucial influence on the transport evolution of blocky debris avalanches. Graben structures or earlier deposits can focus on an elongated transport following the slope instead of a free spreading of blocks along contour lines and earlier deposits may control the transport and evolution of subsequent events. Accurate landslide modeling therefore needs to consider topographic influences on slide dynamics. It is unlikely that these complexities have a significant influence on tsunami generation at Montserrat because of the depth of the Montserrat-Bouillante Graben (>1,000 m), but they have likely more important implications for shallower water settings such as at Anak Krakatau or Ritter Island.

Based on the available high-resolution 3D seismic data sets from volcanic flank collapses at Montserrat and Ritter Island, we suggest that erosive late-stage density currents are a common process during volcanic flank collapse emplacement. This process requires huge amounts of sediment suspended in the water column. The complexity of the subsequent deposits and their emplacement challenges simplified flow models as they are unlikely to reproduce an accurate picture of the depositional sequence. However, simplified models are still useful for assessing tsunami potential as long as they are based upon an estimation of the initial landslide failure volume rather than the final deposit volume, as the initial stage of landslide failure is likely to be the most significant in tsunami genesis.

Data Availability Statement

The geophysical datasets used in this study can be found in the PANGAEA data repository. The 2D seismic data can be accessed via https://doi.org/10.1594/PANGAEA.957490 (Kühn et al., 2023a) and the 3D seismic data via https://doi.org/10.1594/PANGAEA.963076 (Kühn et al., 2023b) and will be downloadable after a moratorium in 04/2025 and 09/2025 respectively. Hydroacoustic data can be accessed via https://doi.org/10.1594/PANGAEA.935598 (Berndt et al., 2021).

References

Auker, M. R., Sparks, R. S. J., Siebert, L., Crosweller, H. S., & Ewert, J. (2013). A statistical analysis of the global historical volcanic fatalities record. *Journal of Applied Volcanology*, 2, 1–24. https://doi.org/10.1186/2191-5040-2-2

Barrett, R., Lebas, E., Ramalho, R., Klaucke, I., Kutterolf, S., Klügel, A., et al. (2020). *Revisiting the tsunamigenic volcanic flank collapse of fogo island in the cape verdes, offshore West Africa* (pp. 13–26). Geological Society Special Publication. Geological Society of London. https://doi.org/10.1144/SP500-2019-187

Berndt, C., Böttner, C., Elger, J., Kontradowitz, S., Kühn, M., Müller, S., et al. (2019). (p. 47). *METEOR-Berichte, M154/1.Sector collapse kinematics and tsunami implications - SEKT, cruise No. M154/1, April 3 - April 25, 2019, mindelo (Cape Verde) - Point-á-Pitre (Guadeloupe)*. Gutachterpanel Forschungsschiffe.

Berndt, C., Böttner, C., & Wölfl, A.-C. (2021). Multibeam bathymetry raw data (Kongsberg EM 122 entire dataset) of RV METEOR during cruise M154/1. https://doi.org/10.1594/PANGAEA.935598

Bouysse, P., & Westercamp, D. (1990). Subduction of Atlantic aseismic ridges and late Cenozoic evolution of the lesser Antilles island arc. *Tectonophysics*, *175*(4), 349–380. https://doi.org/10.1016/0040-1951(90)90180-g

Brunet, M., Le Friant, A., Boudon, G., Lafuerza, S., Talling, P., Hornbach, M., & IODP Expedition 340 Science Party. (2016). Composition, geometry, and emplacement dynamics of a large volcanic island landslide offshore M artinique: From volcano flank-collapse to seafloor sediment failure? *Geochemistry, Geophysics, Geosystems*, *17*(3), 699–724. https://doi.org/10.1002/2015gc006034

Casalbore, D., Clare, M. A., Pope, E. L., Quartau, R., Bosman, A., Chiocci, F. L., et al. (2021). Bedforms on the submarine flanks of insular volcanoes: New insights gained from high resolution seafloor surveys. *Sedimentology*, *68*(4), 1400–1438. https://doi.org/10.1111/sed.12725

Chopra, S., & Marfurt, K. J. (2008). Emerging and future trends in seismic attributes. *The Leading Edge*, *27*(3), 298–318. https://doi.org/10.1190/1.2896620

Clare, M., Chaytor, J., Dabson, O., Gamboa, D., Georgiopoulou, A., Eady, H., et al. (2019). A consistent global approach for the morphometric characterization of subaqueous landslides. *Geological Society, London, Special Publications*, *477*(1), 455–477. https://doi.org/10.1144/SP477.15

Clare, M. A., Yeo, I. A., Watson, S., Wysoczanski, R., Seabrook, S., Mackay, K., et al. (2023). Fast and destructive density currents created by ocean-entering volcanic eruptions. *Science*, *381*(6662), 1085–1092. https://doi.org/10.1126/science.adi3038

Coussens, M. F., Wall-Palmer, D., Talling, P. J., Watt, S. F. L., Hatter, S. J., Cassidy, M., et al. (2016). Synthesis: Stratigraphy and age control for IODP sites U1394, U1395, and U1396 offshore Montserrat in the lesser Antilles. *Proceedings of the IODP*. https://doi.org/10.2204/iodp.proc.340.204.2016

Crutchley, G. J., Karstens, J., Berndt, C., Talling, P. J., Watt, S. F. L., Vardy, M. E., et al. (2013). Insights into the emplacement dynamics of volcanic landslides from high-resolution 3D seismic data acquired offshore Montserrat, Lesser Antilles. *Marine Geology*, *335*, 1–15. https://doi.org/10.1016/j.margeo.2012.10.004

Davies, T. R. H., & Tinker, C. C. (1984). Fundamental characteristics of stream meanders. *GSA Bulletin*, *95*(5), 505–512. https://doi.org/10.1130/0016-7606(1984)95<505:FCOSM>2.0.CO;2

Davis, W. M. (1924). The formation of the lesser Antilles. *Proceedings of the National Academy of Sciences*, *10*(6), 205–211. https://doi.org/10.1073/pnas.10.6.205

Day, S. J., Heleno Da Silva, S. I. N., & Fonseca, J. F. B. D. (1999). A past giant lateral collapse and present-day flank instability of Fogo, Cape Verde Islands. *Journal of Volcanology and Geothermal Research*, *94*(1–4), 191–218. https://doi.org/10.1016/S0377-0273(99)00103-1

De Haas, T., Braat, L., Leuven, J. R. F. W., Lokhorst, I. R., & Kleinhans, M. G. (2015). Effects of debris flow composition on runout, depositional mechanisms, and deposit morphology in laboratory experiments. *J Geophys ResEarth Surface*, *120*(9), 1949–1972. https://doi.org/10.1002/2015JF003525

Elverhoi, A., Breien, H., De Blasio, F. V., Harbitz, C. B., & Pagliardi, M. (2010). Submarine landslides and the importance of the initial sediment composition for run-out length and final deposit. *Ocean Dynamics*, *60*(4), 1027–1046. https://doi.org/10.1007/s10236-010-0317-z

Expedition 340 Scientists. (2012). Integrated Ocean drilling Program expedition 340 preliminary report lesser Antilles volcanism and landslides implications for hazard assessment and long-term magmatic evolution of the arc. *IODP Prel. Report*, *340*. https://doi.org/10.2204/iodp.pr.340.2012

Expedition 340 Scientists. (2013). Expedition 340 summary. In A. Le Friant, O. Ishizuka, & N. A. Stroncik (Eds.), *The expedition 340 Scientists*, *Proceeding of IODP* (Vol. 340). Integrated Ocean Drilling Program Management International, Inc. https://doi.org/10.2204/iodp.proc.340.101.2013

Fannin, R. J., & Wise, M. P. (2001). An empirical-statistical model for debris flow travel distance. *Canadian Geotechnical Journal*, *38*(5), 982–994. https://doi.org/10.1139/cgj-38-5-982

Feuillet, N., Leclerc, F., Tapponnier, P., Beauducel, F., Boudon, G., Le Friant, A., et al. (2010). Active faulting induced by slip partitioning in Montserrat and link with volcanic activity: New insights from the 2009 GWADASEIS marine cruise data. *Geophysical Research Letters*, *37*(19), 1–6. https://doi.org/10.1029/2010GL042556

Ford, J., Camerlenghi, A., Zolezzi, F., & Calarco, M. (2023). Seismic amplitude response to internal heterogeneity of mass-transport deposits. *Solid Earth*, *14*(2), 137–151. https://doi.org/10.5194/se-14-137-2023

Freudenthal, T., & Wefer, G. (2013). Drilling cores on the sea floor with the remote-controlled sea floor drilling rig MeBo. *Geoscientific Instrumentation, Methods and Data Systems*, *2*, 329–337. https://doi.org/10.5194/gi-2-329-2013

Frey-Martínez, J., Cartwright, J., & James, D. (2006). Frontally confined versus frontally emergent submarine landslides: A 3D seismic characterisation. *Marine and Petroleum Geology*, *23*(5), 585–604. https://doi.org/10.1016/j.marpetgeo.2006.04.002

Grilli, S. T., Tappin, D. R., Carey, S., Watt, S. F. L., Ward, S. N., Grilli, A. R., et al. (2019). Modelling of the tsunami from the December 22, 2018 lateral collapse of Anak Krakatau volcano in the Sunda Straits, Indonesia. *Scientific Reports*, *9*, 1–13. https://doi.org/10.1038/s41598-019-48327-6

Grindlay, N. R., Hearne, M., & Mann, P. (2005). High risk of tsunami in the Northern Caribbean. *Eos*, *86*(12), 121–126. https://doi.org/10.1029/2005EO120001

Hansen, L. A. S., Callow, R. H. T., Kane, I. A., Gamberi, F., Rovere, M., Cronin, B. T., & Kneller, B. C. (2015). Genesis and character of thin-bedded turbidites associated with submarine channels. *Marine and Petroleum Geology*, *67*, 852–879. https://doi.org/10.1016/j.marpetgeo.2015.06.007

Harford, C. L., Pringle, M. S., Sparks, R. S. J., & Young, S. R. (2002). The volcanic evolution of Montserrat using ^{40}Ar/^{39}Ar geochronology. *Geological Society*, *21*(1), 93–113. https://doi.org/10.1144/GSL.MEM.2002.021.01.05

Herd, R. A., Edmonds, M., & Bass, V. A. (2005). Catastrophic lava dome failure at Soufrière Hills volcano, Montserrat, 12-13 July 2003. *Journal of Volcanology and Geothermal Research*, *148*(3–4), 234–252. https://doi.org/10.1016/j.jvolgeores.2005.05.003

Hornbach, M. J., Manga, M., Genecov, M., Valdez, R., Miller, P., Saffer, D., et al. (2015). Permeability and pressure measurements in Lesser Antilles submarine slides: Evidence for pressure-driven slow-slip failure. *Journal of Geophysical Research: Solid Earth*, *120*(12), 7986–8011. https://doi.org/10.1002/2015JB012061

Huhn, K., Freudenthal, T., Dehning, K., Gatter, R., Hilgenfeldt, C., Hönekopp, L., et al. (2019). Sector collapse kinematics and tsunami implications - SEKT. Cruise No. M154-2, April 29 - Mai 23, 2019, Pointe-à-Pitre (Guadeloupe) - Pointe-à-Pitre (Guadeloupe).

Karstens, J., Berndt, C., Urlaub, M., Watt, S. F. L., Micallef, A., Ray, M., et al. (2019). From gradual spreading to catastrophic collapse – Reconstruction of the 1888 Ritter Island volcanic sector collapse from high-resolution 3D seismic data. *Earth and Planetary Science Letters*, *517*, 1–13. https://doi.org/10.1016/j.epsl.2019.04.009

Karstens, J., Crutchley, G. J., Berndt, C., Talling, P. J., Watt, S. F. L., Hühnerbach, V., et al. (2013). Emplacement of pyroclastic deposits offshore Montserrat: Insights from 3D seismic data. *Journal of Volcanology and Geothermal Research*, *257*, 1–11. https://doi.org/10.1016/j.jvolgeores.2013.03.004

Karstens, J., Haflidason, H., Berndt, C., & Crutchley, G. J. (2023). Revised Storegga Slide reconstruction reveals two major submarine landslides 12,000 years apart. *Communications Earth & Environment*, *4*(1), 55. https://doi.org/10.1038/s43247-023-00710-y

Karstens, J., Kelfoun, K., Watt, S. F. L., & Berndt, C. (2020). Combining 3D seismics, eyewitness accounts and numerical simulations to reconstruct the 1888 Ritter Island sector collapse and tsunami. *International Journal of Earth Sciences*, *109*(8), 2659–2677. https://doi.org/10.1007/s00531-020-01854-4

Krastel, S., Schmincke, H. U., Jacobs, C. L., Rihm, R., Le Bas, T. P., & Alibés, B. (2001). Submarine landslides around the canary Islands. *Journal of Geophysical Research*, *106*(B3), 3977–3997. https://doi.org/10.1029/2000jb900413

Kühn, M., Berndt, C., & Krastel, S. (2023a). 2D multichannel seismic reflection processed data (GI Gun entire dataset) of RV METEOR during cruise M154/1. https://doi.org/10.1594/PANGAEA.957490

Kühn, M., Berndt, C., & Krastel, S. (2023b). 3D multichannel seismic reflection processed data (P-Cable system with GI Gun) of RV METEOR during cruise M154/1, Montserrat. *Lesser Antilles*. https://doi.org/10.1594/PANGAEA.963076

Kühn, M., Karstens, J., Berndt, C., & Watt, S. F. L. (2021). Seismic reconstruction of seafloor sediment deformation during volcanic debris avalanche emplacement offshore Sakar, Papua New Guinea. *Marine Geology*, *439*, 106563. https://doi.org/10.1016/j.margeo.2021.106563

Kunde, D. (2020). *Seismic velocity of sector collapse deposits off Montserrat (Master's thesis)*. Christian-Albrechts-Universität zu Kiel.

Lebas, E., Le Friant, A., Boudon, G., Watt, S. F. L., Talling, P. J., Feuillet, N., et al. (2011). Multiple widespread landslides during the long-term evolution of a volcanic island: Insights from high-resolution seismic data, Montserrat, Lesser Antilles. *Geochemistry, Geophysics, Geosystems*, *12*(5). https://doi.org/10.1029/2010GC003451

Le Friant, A., Deplus, C., Boudon, G., Sparks, R. S. J., Trofimovs, J., & Talling, P. (2009). Submarine deposition of volcaniclastic material from the 1995-2005 eruptions of Soufrière Hills volcano, Montserrat. *J Geol Soc London*, *166*(1), 171–182. https://doi.org/10.1144/0016-76492008-047

Le Friant, A., Harford, C. L., Deplus, C., Boudon, G., Sparks, R. S. J., Herd, R. A., & Komorowski, J. C. (2004). Geomorphological evolution of Montserrat (West Indies): Importance of flank collapse and erosional processes. *J Geol Soc London*, *161*(1), 147–160. https://doi.org/10.1144/0016-764903-017

Le Friant, A., Ishizuka, O., Boudon, G., Palmer, M. R., Talling, P. J., Villemant, B., et al. (2015). Submarine record of volcanic island construction and collapse in the Lesser Antilles arc: First scientific drilling of submarine volcanic island landslides by IODP Expedition 340. *Geochemistry, Geophysics, Geosystems*, *16*(2), 420–442. https://doi.org/10.1002/2014GC005652

Le Friant, A., Ishizuka, O., & Stroncik, N. A., & the Expedition 340 Scientists. (2013). Site U1395. In *Proceedings of the integrated Ocean Drilling Program*. https://doi.org/10.2204/iodp.proc.340.105.2013

Lenz, B. L., Sawyer, D. E., Phrampus, B., Davenport, K., & Long, A. (2019). Seismic imaging of seafloor deformation induced by impact from large submarine landslide blocks, offshore Oregon. *Geosciences*, *9*(1), 10. https://doi.org/10.3390/geosciences9010010

Løvholt, F., Pedersen, G., Harbitz, C. B., Glimsdal, S., & Kim, J. (2015). On the characteristics of landslide tsunamis. *Philosophical Transactions of the Royal Society A: Mathematical, Physical & Engineering Sciences*, *373*(2053), 20140376. https://doi.org/10.1098/rsta.2014.0376

Masson, D. G., Harbitz, C. B., Wynn, R. B., Pedersen, G., & Løvholt, F. (2006). Submarine landslides: Processes, triggers and hazard prediction. *Philos Trans A Math Phys Eng Sci*, *364*(1845), 2009–2039. https://doi.org/10.1098/rsta.2006.1810

Masson, D. G., Watts, A. B., Gee, M. J. R., Urgeles, R., Mitchell, N. C., Le Bas, T. P., & Canals, M. (2002). Slope failures on the flanks of the western Canary Islands. *Earth-Science Reviews*, *57*(1–2), 1–35. https://doi.org/10.1016/S0012-8252(01)00069-1

McHugh, C. M., Seeber, L., Braudy, N., Cormier, M. H., Davis, M. B., Diebold, J. B., et al. (2011). Offshore sedimentary effects of the 12 January 2010 Haiti earthquake. *Geology*, *39*(8), 723–726. https://doi.org/10.1130/G31815.1

Mohrig, D., Ellis, C., Parker, G., Whipple, K. X., & Hondzo, M. (1998). Hydroplaning of subaqueous debris flows. *GSA Bulletin*, *110*(3), 387–394. https://doi.org/10.1130/0016-7606(1998)110<0387:HOSDF>2.3.CO;2

Moore, J. G., & Normark, W. R. (1994). Giant Hawaiian landslides. *Annual Review of Earth and Planetary Sciences*, *22*(1), 119–144. https://doi.org/10.1146/annurev.earth.22.1.119

Morita, S., Nakajima, T., & Hanamura, Y. (2011). Submarine slump sediments and related dewatering structures: Observations of 3D seismic data obtained for the continental slope off Shimokita Peninsula, NE Japan. *The Journal of the Geological Society of Japan*, *117*(2), 95–98. https://doi.org/10.5575/geosoc.117.95

Noguchi, T., Tanikawa, W., Hirose, T., Lin, W., Kawagucci, S., Yoshida-Takashima, Y., et al. (2012). Dynamic process of turbidity generation triggered by the 2011 Tohoku-Oki earthquake. *Geochemistry, Geophysics, Geosystems*, *13*(11). https://doi.org/10.1029/2012GC004360

Normark, W. R., & Carlson, P. R. (2003). Giant submarine canyons: Is size any clue to their importance in the rock record? *GSA Special Papers*, *370*, 175–190.

Ogata, K., Festa, A., Pini, G. A., & Lucente, C. C. (2019). Substrate deformation and incorporation in sedimentary mélanges (olistostromes): Examples from the northern Apennines (Italy) and northwestern Dinarides (Slovenia). *Gondwana Research*, *74*, 101–125. https://doi.org/10.1016/j.gr.2019.03.001

Ogata, K., Pogačnik, Z., Pini, G. A., Tunis, G., Festa, A., Camerlenghi, A., & Rebesco, M. (2014). The carbonate mass transport deposits of the Paleogene Friuli Basin (Italy/Slovenia): Internal anatomy and inferred genetic processes. *Marine Geology*, *356*, 88–110. https://doi.org/10.1016/j.margeo.2014.06.014

Ryan, W. B. F., Carbotte, S. M., Coplan, J. O., O'Hara, S., Melkonian, A., Arko, R., et al. (2009). Global multi-resolution topography synthesis. *Geochemistry, Geophysics, Geosystems*, *10*(3). https://doi.org/10.1029/2008GC002332

Shen, W., Berti, M., Li, T., Benini, A., & Qiao, Z. (2022). The influence of slope gradient and gully channel on the run-out behavior of rockslide-debris flow: An analysis on the Verghereto landslide in Italy. *Landslides*, *19*(4), 885–900. https://doi.org/10.1007/s10346-022-01848-0

Shepard, F. P. (1981). Submarine canyons: Multiple causes and long-time Persistence. *The American Association of Petroleum Geologists Bulletin*, *65*, 1062–1077. https://doi.org/10.1306/03B59459-16D1-11D7-8645000102C1865D

Silver, E., Day, S., Ward, S., Hoffmann, G., Llanes, P., Driscoll, N., et al. (2009). Volcano collapse and tsunami generation in the Bismarck volcanic arc, Papua New Guinea. *Journal of Volcanology and Geothermal Research*, *186*(3–4), 210–222. https://doi.org/10.1016/j.jvolgeores.2009.06.013

Sobiesiak, M. S., Kneller, B., Alsop, G. I., & Milana, J. P. (2018). Styles of basal interaction beneath mass transport deposits. *Marine and Petroleum Geology*, *98*, 629–639. https://doi.org/10.1016/j.marpetgeo.2018.08.028

Sparks, R. S. J., Barclay, J., Calder, E. S., Herd, R. A., Komorowski, J.-C., Luckett, R., et al. (2002). Generation of a debris avalanche and violent pyroclastic density current on 26 December (Boxing Day) 1997 at Soufrière Hills volcano, Montserrat. *Geological Society, London, Memoirs*, *21*(1), 409–434. https://doi.org/10.1144/GSL.MEM.2002.021.01.18

Thunell, R., Tappa, E., Varela, R., Llano, M., Astor, Y., Muller-Karger, F., & Bohrer, R. (1999). Increased marine sediment suspension and fluxes following an earthquake. *Nature*, *398*(6724), 233–236. https://doi.org/10.1038/18430

Tost, M., Cronin, S. J., & Procter, J. N. (2014). Transport and emplacement mechanisms of channelised long-runout debris avalanches, Ruapehu volcano, New Zealand. *Bulletin of Volcanology*, *76*(12), 1–14. https://doi.org/10.1007/s00445-014-0881-z

Trofimovs, J., Sparks, R. S. J., & Talling, P. J. (2008). Anatomy of a submarine pyroclastic flow and associated turbidity current: July 2003 dome collapse, Soufri??re Hills volcano, Montserrat, West Indies. *Sedimentology*, *55*(3), 617–634. https://doi.org/10.1111/j.1365-3091.2007.00914.x

Trofimovs, J., Talling, P. J., Fisher, J. K., Sparks, R. S. J., Watt, S. F. L., Hart, M. B., et al. (2013). Timing, origin and emplacement dynamics of mass flows offshore of SE Montserrat in the last 110 ka: Implications for landslide and tsunami hazards, eruption history, and volcanic island evolution. *Geochemistry, Geophysics, Geosystems*, *14*(2), 385–406. https://doi.org/10.1002/ggge.20052

Wadge, G., Voight, B., Sparks, R. S. J., Cole, P. D., Loughlin, S. C., & Robertson, R. E. A. (2014). An overview of the eruption of Soufrière Hills volcano, Montserrat from 2000 to 2010. *Geological Society Memoir*, *39*, 1–39. https://doi.org/10.1144/M39.1

Walter, T. R., Haghshenas Haghighi, M., Schneider, F. M., Coppola, D., Motagh, M., Saul, J., et al. (2019). Complex hazard cascade culminating in the Anak Krakatau sector collapse. *Nature Communications*, *10*(1), 4339. https://doi.org/10.1038/s41467-019-12284-5

Ward, S. N. (2001). Landslide tsunami. *Journal of Geophysical Research*, *106*(B6), 11201–11215. https://doi.org/10.1029/2000jb900450

Ward, S. N., & Day, S. (2003). Ritter island volcano - lateral collapse and the tsunami of 1888. *Geophysical Journal International*, *154*(3), 891–902. https://doi.org/10.1046/j.1365-246X.2003.02016.x

Watt, S. F. L., Jutzeler, M., Talling, P. J., Carey, S. N., Sparks, R. S. J., Tucker, M., et al. (2015). New insights into landslide processes around volcanic islands from Remotely Operated Vehicle (ROV) observations offshore Montserrat. *Geochemistry, Geophysics, Geosystems*, *16*(7), 2240–2261. https://doi.org/10.1002/2015GC005781

Watt, S. F. L., Karstens, J., & Berndt, C. (2021). Volcanic-island lateral collapses and their submarine deposits. *Advances in Volcanology*, 255–279. https://doi.org/10.1007/978-3-030-57411-6_10

Watt, S. F. L., Karstens, J., Micallef, A., Berndt, C., Urlaub, M., Ray, M., et al. (2019). From catastrophic collapse to multi-phase deposition: Flow transformation, seafloor interaction and triggered eruption following a volcanic-island landslide. *Earth and Planetary Science Letters*, *517*, 135–147. https://doi.org/10.1016/j.epsl.2019.04.024

Watt, S. F. L., Talling, P. J., Vardy, M. E., Heller, V., Hühnerbach, V., Urlaub, M., et al. (2012). Combinations of volcanic-flank and seafloor-sediment failure offshore Montserrat, and their implications for tsunami generation. *Earth and Planetary Science Letters*, *319–320*, 228–240. https://doi.org/10.1016/j.epsl.2011.11.032

Watt, S. F. L., Talling, P. J., Vardy, M. E., Masson, D. G., Henstock, T. J., Hühnerbach, V., et al. (2012). Widespread and progressive seafloor-sediment failure following volcanic debris avalanche emplacement: Landslide dynamics and timing offshore Montserrat, Lesser Antilles. *Marine Geology*, *323–325*, 69–94. https://doi.org/10.1016/j.margeo.2012.08.002

Yoshida, H., Sugai, T., & Ohmori, H. (2012). Geomorphology Size – Distance relationships for hummocks on volcanic rockslide-debris avalanche deposits in Japan. *Geomorphology*, *136*(1), 76–87. https://doi.org/10.1016/j.geomorph.2011.04.044

Young, S. R., Sparks, R. S. J., Aspinall, W. P., Lynch, L. L., Miller, A. D., Robertson, R. E. A., & Shepherd, J. B. (1998). Overview of the eruption of Soufriere Hills volcano, Montserrat, 18 July 1995 to December 1997. *Geophysical Research Letters*, *25*, 3389–3392. https://doi.org/10.1029/98GL01405